Design and Modeling of a High Reliability Pump for Liquid Cooling Data Center Servers

Elizabeth Grace Rasmussen

A thesis

submitted in partial fulfillment of the

requirements for the degree of

Master of Science

University of Washington

2018

Committee:

Alexander V. Mamishev

Igor Novosselov

Steve Shen

Program Authorized to Offer Degree:

Department of Mechanical Engineering

University of Washington

Abstract

Design and Modeling of a High Reliability Pump for Liquid Cooling Data Center Servers

Elizabeth Grace Rasmussen

Chair of the Supervisory Committee:
Professor Alexandar V. Mamishev
Department of Electrical Engineering

Data center buildings are tasked with safely housing a large number of temperature sensitive components found in computer servers. These industrial buildings consume about 1.3% of the world's electrical energy, of which about 40% is spent on cooling [1, 2]. Current cooling strategies fail to meet the heat transfer requirements of current microprocessors due to high heat fluxes resulting from increased component density and decreased device size. The goal of this study is focused on the design and modeling of a high-reliability pump that can be used at the data center server board-level source of the heat flux. The design includes a shaft-less pump design, an external magnetic drive, and a self-adjusting position of the rotor driven by a herringbone grooved fluid bearing. A proof-of-concept prototype of the design was built and tested using a flow meter. The manufacturing of the pump's rotor, chassis, and stator was all accomplished using the Fused Deposition Modeling three-dimensional (3D) printing technique. Best practices for dimensional accuracy of 3D printed herringbone groove geometries are revealed for both plastic and composite filament material. The electrical properties of composite metal filament are also discussed. The anticipated benefit of this project is to increase the use of liquid cooling used in data center servers replacing passive air-cooled heat sinks. By doing this a large reduction in the overall electrical power consumption currently required by data centers can be achieved.

TABLE OF CONTENTS

List of Figures iv

List of Tables vii

Chapter 1. Introduction 1

1.1 Significance of Thermal Management in Data Center Network Servers 1

1.1.1 The Problem 1

1.1.2 The Significance 1

1.1.3 The Solution 3

1.2 Engineering and Scientific Challenges 4

1.3 Scope of the Thesis 5

1.4 Contributions of the Thesis 7

1.5 Outline of the Thesis 8

Chapter 2. Review of Fundamental Concepts 9

2.1 Fundamentals Behind Liquid Cooling 9

2.1.1 Energy Saving Potential 9

2.1.2 Data Center Environment Operating Conditions 11

2.2 Introduction to Herringbone Groove Theory 11

2.2.1 Governing Equations 11

2.2.2 Literature Review of Herringbone Grooves 16

2.3 Introduction To BLDC Motor Theory 17

2.3.1 Governing Equations 19

Chapter 3. System Design 22

3.1 Pump Rotor 22

3.1.1 Herringbone Grooves 22

3.1.2 Internal Permanent Magnets 23

3.1.3 Design 24

3.2 Chassis 26

3.2.1 Water Retention Testing and Material Selection 26

3.2.2 Design 28

3.3 Stator 30

3.3.1 Stacked Steel Shim Design 30

3.3.2 Iron Composite PLA Design 32

3.4 Pump System's Fluid Circulation Loop 34

3.5 Summary 36

Chapter 4. System Experiment 38

4.1 Materials and Methods 38

4.1.1 Three-Dimensional Printing 38

4.1.2 Optical Images of Parts 41

4.2 Experimental Setup 43

4.3 Results and Discussion 45

4.3.1 Surface Roughness of 3D Printed Parts 45

4.3.2 Pump Rotor 46

4.3.3 Pump Chassis 47

4.3.4 Pump Stator 48
4.3.5 Pump Fluid Assembly 49
4.3.6 Functional Testing 49
Chapter 5. Conclusions and Future work 51
5.1 Conclusions 51
5.2 Future Work 51
5.2.1 Research 51
5.2.2 Commercialization 53
Bibliography 55
Appendix A: Nomenclature 61
Appendix B: Functional Test Results 63

LIST OF FIGURES

Figure 1: (A) Outside view of a data center with air conditioning systems highlighted (i) cooled air handling units (ii) roof-mounted air-cooled chillers (iii) evaporative cooling towers. (B) Inside view of a data center showing computer server isles that generate large loads of heat and (i) internal Computer Room Air Handler units 2
Figure 2: Photograph of a heat sink installed over a CPU [7] 2
Figure 3: Photograph showing a computer server's CPU that is smoking from poor thermal management and thus overheating and breaking of the CPU [8] 3
Figure 4: Scope of the thesis and future work. 6
Figure 5: A head to head comparison of cooling technologies available in the data center server industry..... 10
Figure 6. Schematic of the grooved journal (rotor) inside of a sleeve (chassis) with key coordinate system components identified. 12
Figure 7. Schematic of (top) square groove geometry (middle) circular groove geometry (bottom) bevelled-step groove geometry with control surface '*abcd'* specified. 14
Figure 8. Schematic of the unwrapped geometry of herringbone grooves showing the groove and ridges..... 14
Figure 9. Schematic of a close-up view of a herringbone groove design with key geometry features identified..... 15
Figure 10. Schematic of the cross-section X-X of a bevelled-step herringbone groove. . 15
Figure 11. Schematic of 12 tooth, 3 phase BLDC motor with an inner rotor core containing 10 permanent magnets. 18
Figure 12. Commutation sequence for a three-phase BLDC motor 19
Figure 13: Overview of the rotor design highlighting herringbone groove stability design features, rotor fins, and coolant flow direction through the shaftless rotor. 25
Figure 14: CAD images of the rotor as one piece and then split to create a top and bottom piece T1) the top piece of the split rotor in the same orientation as the whole rotor piece T2)

Upside down view of T1 B1) the bottom piece of the split rotor in the same orientation as the whole rotor B2) Upside down view of B1 26
Figure 15. A photograph showing the PLA plastic 3D print specimens organized by 3D printing layer resolution in all three ASTM D570-98 (2010) standard sizes. 27
Figure 16. Design of the chassis with parts and major sections outlined. 29
Figure 17. Front section view of the chassis CAD model showing top, front, and orthogonal views of the final stator assembly design with key dimensions noted..... 30
Figure 18. Photograph of the 6 teeth first iteration design where 72 steel shims were stacked to create the body of the stator. 31
Figure 19. Close up photographs of wire insulation on stator removed from rough edges of the stator..... 32
Figure 20. Solidworks CAD model of stator cross section..... 33
Figure 21. Images of the CAD model showing top, front, and orthogonal views of the final stator assembly design with key dimensions highlighted. 34
Figure 22. Photograph of the Thermaltake Aqua TMG1 radiator with inlet and outlet locations identified 35
Figure 23: Assembled view of the proposed pump design installed on a motherboard in a server. 36
Figure 24: A 3D computer aid design section view of the pump design, outlining key design components and highlighting the heat transfer between the CPU and the fluid flowing through the pump's assembly. 37
Figure 25: Photograph of the power washing station used to remove Objet Support SUP707 material from samples printed using PolyJet technology. 39
Figure 26: Orthogonal views of the two 3D CAD model geometries printed (a) cylinder and (b) square models for square herringbone grooves..... 40
Figure 27: Optical image of tilted FDM square herringbone groove part printed at a 100 µm layer resolution..... 41
Figure 28: Image highlighting granular support material in herringbone grooves. 42

Figure 29. Images of medium and fine-resolution FDM herringbone groove parts (a) 60 µm bevelled-step groove (b) 60 µm square groove (c) 100 µm resolution bevelled-step groove (d) 100 µm resolution square groove. 43
Figure 30: Photograph of the liquid cooling pump tilted upside down and with a section of the chassis base removed to highlight the pump's rotor. 44
Figure 31: Photograph of the experimental setup for testing the proof-of-concept prototype 44
Figure 32. Graph of surface roughness for the chassis with a found surface roughness value, Ra, of 0.562 µm and mean deviation of the 3D printed layers from the nominal height of 3.229 µm. 45
Figure 33. Images of the final rotor prototype showing a) the top half of the rotor b) the top half of the rotor flipped upside down c) the top half of the rotor with section d) close up of the rotor showing the detail of print for the bevelled-step herringbone grooves. 46
Figure 34. Photograph of the final chassis prototype 47
Figure 35. Photograph of the final 3 phase brushless DC motor stator prototype 48
Figure 36. Graph of the functional data collected on Day 1 of testing the prototype 50

LIST OF TABLES

Table 2-1: Overview of the project's potential energy and monetary savings [27]. 9
Table 2-2. Optimum Parameters for Square, Circular, and Beveled-Step Herringbone Grooves. 17
Table 3-1. Magnetic characteristics of the Neodymium arc magnets inside the Rotor 24
Table 3-2 Properties of Proto-pasta's magnetic Iron Metal PLA Composite 32
Table 4-1. 3D Printers Used for Prototypes 39
Table 4-2. Outline of Square, Circular, and Beveled-Step Herringbone Groove Depths and Journal Clearance 40
Table 5-1. Experimental Results from Day 1 of Functional Testing 63
Table 5-2. Experimental Results from Day 2 of Functional Testing 64
Table 5-3. Experimental Results from Day 3 of Functional Testing 65

ACKNOWLEDGEMENTS

The successful completion of this project would not have been possible without the guidance and support from a number of individuals and institutions.

First, I would like to thank my advisor, Alexandar V. Mamishev for giving me the opportunity to join his laboratory, mentoring me through this direction once I joined, and providing research funding. I would also like to express my appreciation to all committee members, Professor Igor Novosselov, and Professor Steve Shen for providing me with insightful comments on my research. Furthermore, I would like to thank my fellow Sensors Energy and Automation Laboratory (SEAL) teammates: Sep Makhsous, Aaron Zielinski, Philip Rudolph, Karl Kintner-Meyer, Molly Foley, and Jon Day.

Additionally, I would like to thank the American Public Power Association (APPA) Demonstration of Energy and Efficiency Developments (DEED) program, Silicon Valley Power, and the Washington Research Foundation for their financial support of this project, without which this work would not be possible.

Finally, I would like to thank all my friends and family, especially my mother, and my husband, Keagan, who have encouraged me through this journey. I feel very blessed to have you all a part of my life and look forward to continuing creating the future with you.

DEDICATION

To all my former public-school teachers. Especially my orchestra teacher, Mrs Karen Viele, and mathematics teacher, Mr Sean V Murray.

Chapter 1. INTRODUCTION

1.1 Significance of Thermal Management in Data Center Network Servers

1.1.1 *The Problem*

Modern technology requires the storing and processing of unprecedented volumes of data. As a result, the number of data centers continues to grow worldwide. Data centers consume increasingly larger amounts of energy as the demand for high-performance data storage continues to escalate [1, 2]. About forty percent of all energy consumed by data centers is spent on the cooling of buildings that house data center electronics [3]. This energy expenditure negatively affects the environment, contributing to air pollution and greenhouse gas emissions [4].

1.1.2 *The Significance*

Existing electronics cooling systems require that data centers are air conditioned down to quite low temperatures, typically about 65°F. While it may not seem like a very low set point, bear in mind that it is applied to the air inside the building that is densely packed with electronic components that constantly produce heat throughout the entire building volume. A low temperature set point is needed to maintain the temperature difference between the air and the radiators attached to the hottest elements, such as the Central Processing Units (CPU). If the temperature difference between the building air and heatsink is too small, the microprocessor will overheat and then slow down, shut down, or fail. Figure 1 shows the massive air conditioning infrastructure in a data center needed both outside and inside the building.

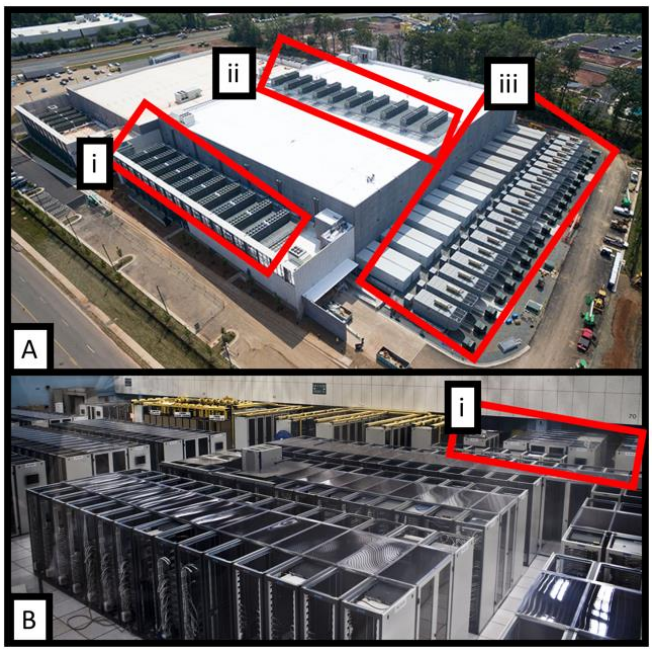

Figure 1: (A) Outside view of a data center with air conditioning systems highlighted (i) cooled air handling units (ii) roof-mounted air-cooled chillers (iii) evaporative cooling towers. (B) Inside view of a data center showing computer server isles that generate large loads of heat and (i) internal Computer Room Air Handler units

The existing practice is to cool high heat density electronic components by attaching them to passive heat sinks, sometimes enhanced by heat pipes between the components and the heat sinks as can be seen in Figure 2 [5-7].

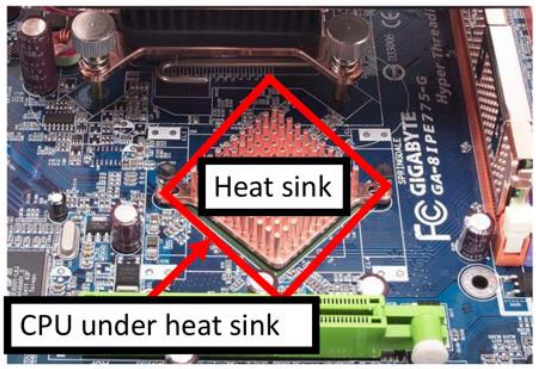

Figure 2: Photograph of a heat sink installed over a CPU [7]

If the thermal management of high heat electronics fails to regulate the temperature not only can the component fail, but in extreme cases can cause smoking and lead to a fire. In Figure 3 a photograph of a Computer Processing Unit that has broken and is now smoking due to poor thermal management.

Figure 3: Photograph showing a computer server's CPU that is smoking from poor thermal management and thus overheating and breaking of the CPU [8]

The advantage of passive heat sinks is that they are very reliable: there are no moving parts, no risk of corrosion, and the only area of concern is maintaining a large contact surface between the heat sink and the chip. The disadvantage is that passive heatsinks are not very efficient at spreading heat [9]. Therefore, a relatively high volume of chilled air needs to pass over the passive heatsink. If the passive heatsink were to be replaced by a liquid cooled heat sink, and, with no changes to the server's air flow paths, it would be possible to increase the air temperature and decrease the flow rate in existing server buildings and server rooms [10]. If the server rack and server room were designed assuming liquid cooling for all CPUs, then even more energy savings would be possible.

1.1.3 *The Solution*

There are no liquid cooling pumps on the market at a cost and size suitable for data centers that also have a long enough operating lifespan. Our solution is to move away from traditional design methods (e.g., axel-and-bearing designs) and instead build a levitating rotor pump. This project represents the first use of fluid bearings with no pump seals in a board-level cooling pump and the first to use symmetrical fluid flow and optimized motor control for dynamic rotor position

control. The pump's rotor is designed to have no surface-to-surface contact between the moving parts, as well as no pump seals; this is achieved using fluid bearings created by herringbone grooves with a net zero radial force on the rotating rotor. Thus, with our proposed solution, although one still needs to air condition the building, this pump would make one need to do significantly less of it, thereby reducing their overall energy consumption [11].

Regarding the market size for the high reliability pump device, it was defined by analysts at BCC Research that the thermal solution hardware market for semiconductor microchip components was $4.6 billion per year in 2017 and is expected to grow at a compound annual growth rate of 6% annually [12]. In the computer market, our focus segment is high-performance computers and data centers. The addressable market in the computer industry is 20 million units a year [6, 13]. For high heat density semiconductors in industrial and military cooling of CPU's, power amplifiers, power conversion in wind turbines, solar cells, and electric vehicles, the market grows to an additional 100 million units per year. The larger market is less demanding regarding reliability but is facing a growing issue with thermal margins. Heat sink vendors could be the potential buyers of the high reliability pump technology or pump products. Given the size of the problem and the known market size the validity of creating such a device is justified from the business economics, environmental, and engineering viewpoints.

1.2 Engineering and Scientific Challenges

Liquid-to-chip cooling at the board-level brings massive energy savings and improved electronics performance. However, more than 85% of the server industry still uses air cooling at the board-level. The main obstacle that prevents a transition from air cooling to liquid cooling is the liquid cooling pump's reliability [14-16]. While reliable pumps do exist at the macro-scale—they rely on fully enclosed bearings to carry the pump on a shaft. Conversely, previous attempts have failed to create a small, yet still reliable, pump on a shaft, leading to no transition to real products as the friction forces bring down the performance and longevity of these kinds of devices [17].

Thus, the first innovation is to move away from axel-and-bearing designs and use a levitating rotor pump. To achieve a reliably long operating life, the pump's rotor is designed to have no surface-to-surface contact between the moving parts and no pump seals. To do this the

pump's rotor will operate under stable dynamic equilibrium; that is, when the rotor deviates from the center position, it will return to the equilibrium position due to a balance of forces caused by the herringbone groove that cause a net zero radial force on the rotating rotor [18].

Additionally, before this project there had been no experimental work completed on creating herringbone groove profiles in a cylinder shape like that found in a journal bearing rotor using 3D printing. The author's work on this subject was shared with the greater scientific community through a published paper and the findings, in turn, were applied to the experimental section of this thesis [19].

1.3 Scope of the Thesis

This thesis focuses on the design and modeling of a proof-of-concept prototype of a liquid pump with (1) a frictionless levitating rotor that (2) utilizes herringbone grooves for stability. Coupling these two novel design elements together in a single design is sought to create a new high-reliability pump. A pictorial depiction of the scope of the thesis can be seen in Figure 4.

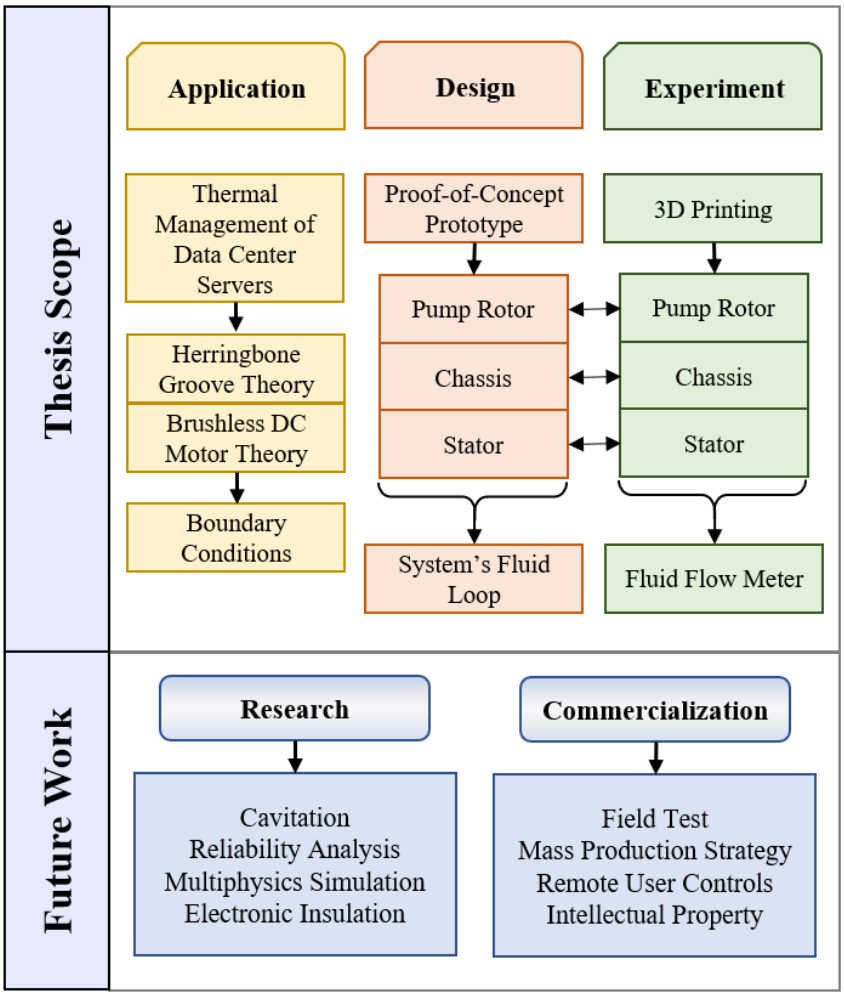

Figure 4: Scope of the thesis and future work.

Application. The intended end use application for this high-reliability pump design is for an industrial *data center server* environment. This specific application was chosen for its relation to the massive potential energy savings due to the currently inefficient thermal management practices within these large industrial buildings. To create a rotor that had no friction with other moving parts in the pump assembly, specifically the chassis or a shaft, the electromagnetic forces involved with *brushless direct current motor theory* between the stator and rotor were employed that allowed the rotor to levitate. To re-center the pump rotor in the case of whirl effect caused by eccentricity *herringbone groove theory* was employed that created two fluid bearings on the top and bottom of the pump rotor. With the selection of these tools, the boundary conditions for the pump system are defined.

Design. There are two main design aspects of this thesis. The first aspect involves the creation of a Computer Aid Design (CAD) model of the proof-of-concept pump rotor, chassis and stator prototype based on the pre-defined application boundary conditions. Second, using the design parameters defined for the pump's rotor, chassis and stator, the pump system's fluid loop was designed using off the shelf components such as a radiator, tubing, and connectors. Readily available permanent magnet rotor magnets were used for implantation into the pump's rotor. Since the goal is a proof-of-concept prototype custom magnets and the various design changes that could be brought about by the use of user-defined size and pull strength parameters was out of the scope of this thesis. Regarding the heatsink selection, although research has been conducted on optimizing fluid flow to maximize heat removal since this is a rapidly evolving field the selection of an optimum heat sink as well as optimizing fluid flow for the heat sink is out of the scope of this body of work [20-23]. Additionally, as there are many different coolant fluids available on the market for use in liquid cooling this thesis focuses on water being the working fluid, the study of flow for fluids beyond water is beyond the scope of this thesis [24, 25].

Experiment. For the experimental portion of this thesis, the manufacturing method for the pump prototype is three-dimensional (3D) printing. The imperfections of this method made the design and experiment process iterative as small flaws in the printed part could cause failure of the prototype to function as intended. Later stages beyond the scope of this project could address other manufacturing methods such as plastic injection modeling. Once optimal 3D printing parameters were found, and the fluid loop was created, and an in-line flow meter was used to measure the pump's capabilities.

1.4 CONTRIBUTIONS OF THE THESIS

This thesis makes a major contribution that attempts to move reliable board level liquid to chip cooling a step forward towards large-scale industrial data center applications.

The innovative features of the approach, belong to the fields of specific applications, including 1) a shaft-less pump design, 2) an external magnetic drive, and 3) a self-adjusting position of the rotor driven by a fluid bearing. The generic ideas of this design are already part of

the field with the most common example being found in the rotation of hard drives in personal computers. The use of liquid bearings in the computer hardware industry is well-established; between 2001 and 2007, they replaced the ball bearings in hard drives, significantly improving their performance and life. In this project, the combination of the three fields outlined is used for the specific application of liquid-to-chip cooling of servers in data centers. The intricacies of a data center application are uniquely complex to warrant a design of a new device. There are no pumps on the market designed for the liquid-to-chip cooling in data centers that offer an operating lifetime equal to that of the computer components.

1.5 Outline of the Thesis

This thesis is broken into five parts.

Chapter 1 introduces the significance of thermal management in data center network servers. The advantages and disadvantages of using liquid-to-chip board level cooling are also discussed. Engineering and Scientific challenges, the scope of the thesis, and the contributions this gives to furthering this sector are included in this chapter as well.

Chapter 2 begins with a review of the fundamentals driving current liquid cooling practice as well as the market saturation limitations. This leads to the innovative solution of utilizing herringbone grooves along a liquid cooling pump's rotor in order to increase stability and possibly lead to the implementation of such a design in the real world.

Chapter 3 presents the overall system design of this high reliable liquid cooling pump. Covering the design of the pump rotor, chassis, and stator

Chapter 4 presents experimental results of the high-reliability pump system design including a detailed analysis of a proof-of-concept prototype and functioning lab set up. Additionally, flow meter data reports the operating conditions of the system while infrared imaging validates thermal operating boundary conditions.

Chapter 5 is the final part of this thesis and contains conclusions and future work. An overview of the work completed is compiled in a table at the beginning of this chapter comparing the results of this thesis work to currently available products. A discussion on several topics of future work is addressed from both research and commercialization points of view.

Chapter 2. REVIEW OF FUNDAMENTAL CONCEPTS

2.1 FUNDAMENTALS BEHIND LIQUID COOLING

The heat generated at the server's component level is first carried away into the building's air through heatsinks and fans and then, eventually, exchanged with the atmosphere, often with the aid of ponds, fountains, and chilling towers [10]. The rate of heat removal is proportional to the temperature differential: cooler air allows for more intensive heat removal from electronic components [13, 26]. At the same time, a very large amount of energy is lost at the interface between the air cooled from inside the building envelope and the hot outside ambient air temperature. Heat dissipation is a multi-stage process that, at the simplest approximation, functions as so: from the chip surface to the heat sink, from the heat sink to the air inside the building, and from the air inside the building to the outdoor air [17].

2.1.1 *Energy Saving Potential*

Given the low thermal capacity of air, a high volume of chilled air needs to pass over the passive heatsink. If the passive heatsink is replaced by a liquid cooled heat sink, and, with no changes to the server's air flow paths, it would be possible to reduce both the air temperature and flow rate in existing servers and server rooms [10]. If the server rack and server room were designed assuming liquid cooling for all CPUs, then even more energy savings would be possible [9]. The device design covered in this thesis falls into the red highlighted "Liquid to the Chip" method seen in Figure 5 where the cooling overhead power consumption is reduced from the "Standard Air-Cooling" method by over 60%.

Table 2-1: Overview of the project's potential energy and monetary savings [27].

Scope:	Global	Country - USA	Washington State
Energy Savings	$85x10^{15}$ kWh	$1.87x10^{11}$ kWh	$4.51x10^{4}$ kWh
Monetary Savings	$5 Billion USD (12 cents/ kWh)	$1.8 Billion USD (7.24 cents/kWh)	$207 Million USD (4.66 cents/kWh)
Magnitude of Savings	Enough energy saved to power the country of Finland for one year	Enough energy saved to power the city of Los Angeles for two years	Enough energy saved to power the city of Seattle for one year

According to a benchmark study of 22 data centers, when liquid-to-chip thermal management is used in data centers, the building's ambient air temperature can be set to 75 °F instead of 65 °F, saving a massive amount of energy. These energy savings are quantified in Table 2-1 [28].

Additionally, a second review study conducted in 2015, testing three data centers and two high-performance computer labs, found the introduction of liquid-to-chip cooling led to the reduction of air conditioning costs by 50% as the overall system thermal margins were increased [1, 3, 6]. Overall, the cost of adding liquid cooling solutions have been proven to have less than a one-year payback based on the savings of electrical energy. A comparison of the power consumption between different methods of precision cooling solutions can be seen in Figure 5. Thus, there is an enormous incentive for data centers to adopt board-level liquid cooling. However, every time there is a decision that concerns which method of precision cooling is used in a data center, the low reliability of existing liquid-to-chip solutions eliminates it as a feasible option for an industry integration. Business losses due to reduced availability of data center service to business clients are too high when motherboards fail from over-heating; therefore, the existing practice is to cool the entire data center building with disproportionally large air conditioning units and chilling towers.

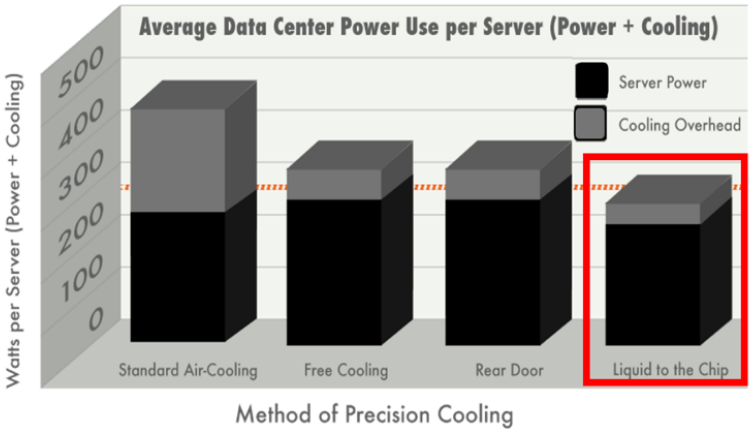

Figure 5: A head to head comparison of cooling technologies available in the data center server industry.

2.1.2 *Data Center Environment Operating Conditions*

Research was completed to define the pump design would be able to operate under when installed on a server for use in a data center. This information is helpful to set boundary conditions in future simulations, and reliability testing.

2.1.2.1 Vibration/Shock Sources

It was found that nearby construction sites, airports, trains, severe weather, earthquakes, as well as internal equipment can all be sources of shock vibration to the server board level environment [29]. Besides these shock vibration forces, it has been found that low-frequency seismic waves are generally more destructive than higher frequency vibration. Regarding the limits of such vibrations research defined peak accelerations greater than 0.5g in servers can results in permanent damage and loss of data [30]. Furthermore, studies have reported the frequency response function of disk/spindle systems with a hydrodynamic bearing [31, 32]. Some mechanisms that can be used to protect the server and in turn the liquid cooling pump are springs, anti-vibration metallic frame, and floating slab floor isolation [33, 34]. These studies should be used for accelerated lifetime reliability testing of a server board liquid cooling system installed in a data center to ensure proper function of both the cooling system and components that it interacts with when installed.

2.1.2.2 Lifetime

The ASHRAE design handbook places a high dependence on the structural components surrounding the data center. In a section outlining building configuration and equipment range it is stated that “the typical refresh rate of datacom equipment is often three to five years [35].” This means that a thermal management system solution should last a minimum of this time span to be successfully implemented in a data center environment.

2.2 INTRODUCTION TO HERRINGBONE GROOVE THEORY

2.2.1 *Governing Equations*

In Figure 6 is shown the coordinate system of a herringbone-grooved journal bearing and plain shaft (chassis in the case of this thesis) that will be used thorughout this thesis.

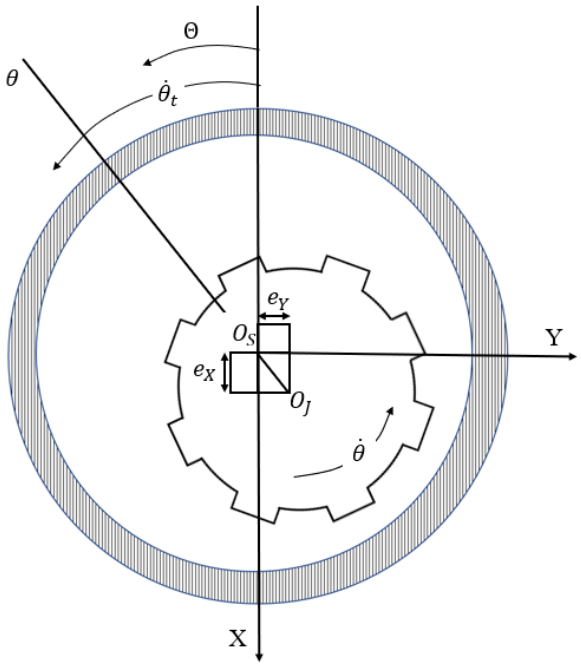

Figure 6. Schematic of the grooved journal (rotor) inside of a sleeve (chassis) with key coordinate system components identified.

From the fixed negative X-axis the circumferential coordinate, Θ, is determined. From here the general Reynolds equation which can be seen in Equation 2.1 can be fixed to the journal ($x' = R\theta, z'$) leading to the following Reynolds equation seen in Equation 2.2 for a grooved journal plain shaft [36].

$$\frac{\partial}{\partial x}\left(\frac{ph^3}{12\mu}\frac{\delta p}{\delta x}\right)+\frac{\partial}{\partial y}\left(\frac{ph^3}{12\mu}\frac{\delta p}{\delta y}\right) = \frac{\partial}{\partial x}\left(\frac{ph(u_a+u_b)}{2}\right)+\frac{\partial}{\partial y}\left(\frac{ph(v_a+v_b)}{2}\right)+\rho(w_a+w_b) - \rho u_a\frac{\delta h}{\delta x} - \rho v_a\frac{\delta h}{\delta y}+h\frac{\delta \rho}{\delta t} \tag{2.1}$$

$$\frac{\partial}{\partial x'}\left(\frac{h^3}{12\mu}\frac{\delta p}{\delta x'}\right)+\frac{\partial}{\partial z'}\left(\frac{h^3}{12\mu}\frac{\delta p}{\delta z'}\right) = -\frac{R\dot{\theta}}{2}\frac{\partial h}{\partial x'}+\frac{\delta h}{\delta t} \tag{2.2}$$

The thickness of the fluid film can be expressed in terms of Θ in the groove region, Equation 2.3, and the ridge region, equation as can be seen in Equation 2.4.

$$h = H_g + H_r + e_X \cos(\Theta) + e_Y \sin(\Theta) \tag{2.3}$$

$$h = c + e_X \cos(\Theta) + e_Y \sin(\Theta) \tag{2.4}$$

Where H_r, H_g, e_X, *and* e_Y are clearance, groove depth and eccentricity in the X and Y directions, respectively. Additionally, the circumferential coordinate can be expressed in terms of the rotational velocity and angular coordinate as can be seen in Equation 2.5.

$$\Theta = \theta + \dot{\theta} t \tag{2.5}$$

To examine the effects of herringbone groove parameters, herringbone geometry and print resolution, understanding the basic geometry of journal bearings and theoretical calculations of the pressure recovery across the herringbone grooves must be understood to create a basis of comparison between a theoretical simulation result and in practice model builds. The first equations that does this are the equation for the pressure drop across a groove profile by Vennard shown below in Equation 2.6 [37].

$$\frac{(P_2 - P_1)}{\gamma} = \frac{V_1^2 - V_2^2}{2g} - (K_L \frac{(V_1 - V_2)^2}{2g}) \tag{2.6}$$

Where P_1 and P_2 are the pressure at position 1 and 2 respectively, γ is the weight density of the fluid, g is the gravitational acceleration, and K_L is the head loss coefficient. The value for K_L is about equal to unity for an abrupt change in the fluid film thickness as experienced in a square herringbone groove profile. Whereas for a circular or beveled-step groove profile where there is a more gradual enlargement of the fluid film thickness the value for K_L is less than unity. The control surface used in Equation 2.6 that encloses the zone of momentum change for a unit axial direction can be seen shown in Figure 7.

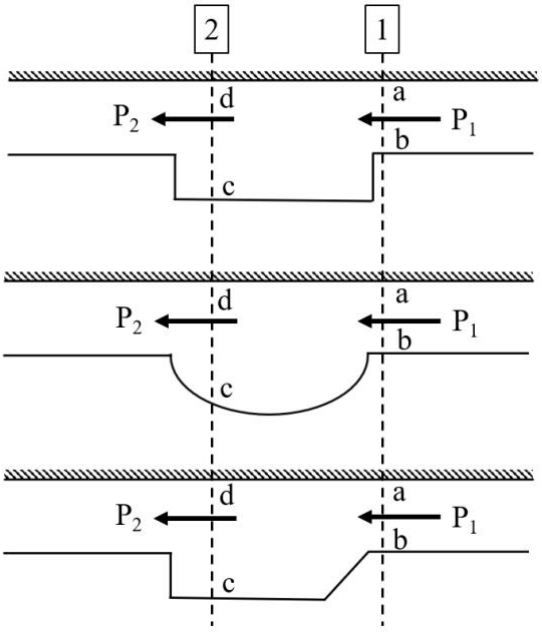

Figure 7. Schematic of (top) square groove geometry (middle) circular groove geometry (bottom) bevelled-step groove geometry with control surface '*abcd'* specified.

The basic geometry parameters for herringbone grooves can be seen in the unwrapped geometry of a journal bearing in Figure 8.

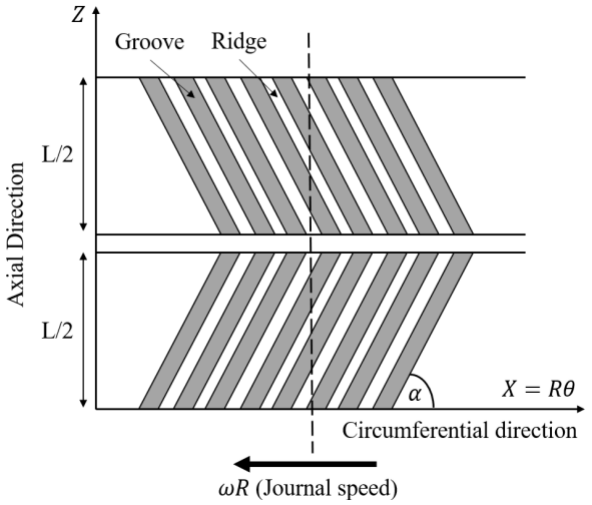

Figure 8. Schematic of the unwrapped geometry of herringbone grooves showing the groove and ridges

A close look at the grooves can be seen in Figure 9 where additional components of herringbone groove geometry are identified including the groove angle, α and axis's.

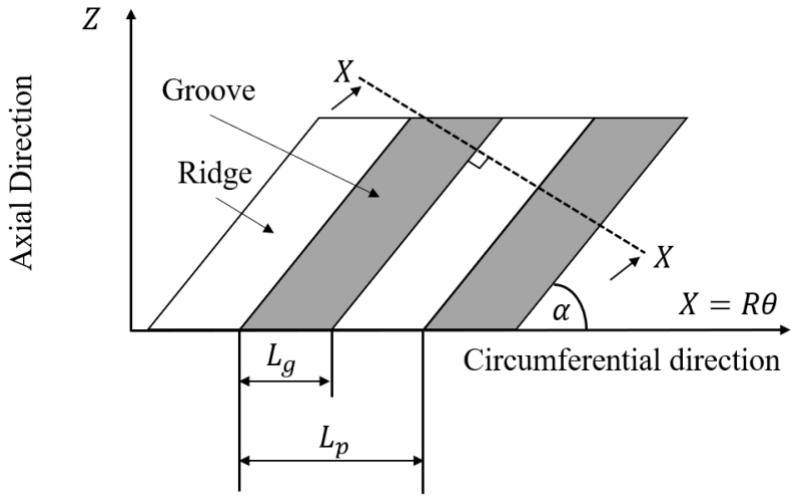

Figure 9. Schematic of a close-up view of a herringbone groove design with key geometry features identified

The cross-section of the groove shown in Figure 9 X-X can be seen in Figure 10. Nomenclature for all sections of this thesis can be seen in Appendix A. Given optimum groove geometries discussed in the upcoming sections the main parameter that will be evaluated in this thesis will be the groove depth, H_g and will subsequently change the distance between the rotor and the stator as defined by H_r.

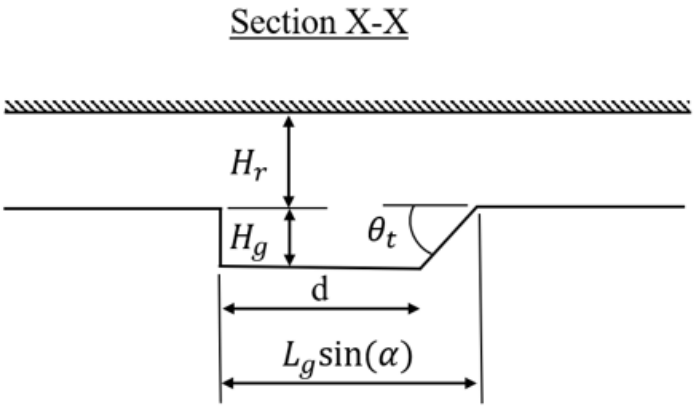

Figure 10. Schematic of the cross-section X-X of a bevelled-step herringbone groove.

The last part of herringbone groove theory that is applicable to this thesis is the minimum number of grooves, *N*, that can be placed on the journal, or rotor, such that the infinite groove analysis yields invalid results which can be seen in Equation 2.7 [38]. Where Λ, is the bearing compressibility number and is defined in Equation 2.8.

$$N = \frac{\Lambda}{5} \tag{2.7}$$

$$\Lambda = \frac{6\mu\omega R^2}{p_a H_R^2} \tag{2.8}$$

2.2.2 *Literature Review of Herringbone Grooves*

The introduction of grooved geometries being applied to a bearing's surface was done in 1958 by Whipple [39]. This was the first lead into producing a pressure distribution for journal stability. Proceeding this introduction, there was much research into the optimum parameters of herringbone grooves on journal bearings and their effects on the concentric operation of the journal bearing. Vohr and Chow noted the optimum groove parameters for square herringbone groove geometry, as listed in Table 2-2, that give maximum radial force, maximum radial stiffness and help inhibit the whirl instability that is common to many self-acting journal bearings [40]. Further, Vohr and Chow explained the ability of herringbone grooves to increase pressure toward the center of the journal bearing causing the journal bearing to remain concentric. To obtain these optimum herringbone groove parameters, the narrow groove theory was introduced which assumes the number of herringbone grooves approaches infinity. Although the narrow groove theory is simple for small eccentricity ratios and large numbers of grooves on a given surface, the finite element method has been employed by many other authors to consider the effect of the groove profile in an array of industry applications in both 2D and 3D simulations [41-46].

Gad et al. followed the lead of other authors such as Kang et al. in investigating the performance of a circular groove, as well as introducing a bevelled-step herringbone groove profile [41, 47]. The primary achievement of the Gad et al.'s investigation was to improve the journal bearing load capacity and stability. Since square and circular groove profiles were found experimentally to have a low load carrying capacity, the bevelled-step groove profile was

investigated heavily for its high load carrying capacity. For the current investigation, the operating conditions resembled Fleming and Bedrock's analysis for low compressibility fluid and a length to diameter ratios of 1. The optimum groove parameters for circular herringbone grooves and bevelled-step herringbone grooves are noted in Table 2-2.

Table 2-2. Optimum Parameters for Square, Circular, and Beveled-Step Herringbone Grooves.

	Key Design Parameters			
Groove Geometry	**Groove angle (α)**	**Groove width ratio (β)**	**Groove depth ratio (Γ)**	**Length to diameter ratio (L/D)**
Square [48]	32.8°	0.5	2.1	1
Square [49]	28.62°	0.5228	2.219	1
Circular [47]	28°	0.25	2.5	1
Beveled-Step [41]	29°	0.5	2.0	1

In comparison to bearings optimized to maximize load carrying capacity, Fleming and Bedrock experimentally determined herringbone groove parameters optimized for maintaining the stability of a square herringbone grooved journal bearing which is why there is a second optimized design parameter being listed for the square groove geometry [49]. Fleming and Bedrock produced results for optimized herringbone grooved journal bearings for a wide array of operating conditions vary in fluid compressibility number, length to diameter ratios, and smooth versus grooved journal bearings.

2.3 Introduction To BLDC Motor Theory

Brushless DC (BLDC) motors have been growing in popularity due to their high efficiency, reliability, and ability to be used in a variety of applications. BLDC motors have distinct

advantages over brushed motors due to lack of brushes, higher life expectancy and flat speed torque characteristics.

The fundamental operation of a BLDC motor relies on the conversion of electrical energy, to magnetic energy, and then to mechanical energy. The stator, or outer ring of the motor as shown in Figure 11, contains 12 “teeth” that conducting wire is wrapped around. These wires are driven by current, creating magnetic north and south poles at positions ABC and A’B’C’ respectively, under the principles of Ampere’s law. The rotor has its own permanent magnet that is repelled by these magnetic fields, and this creates torque.

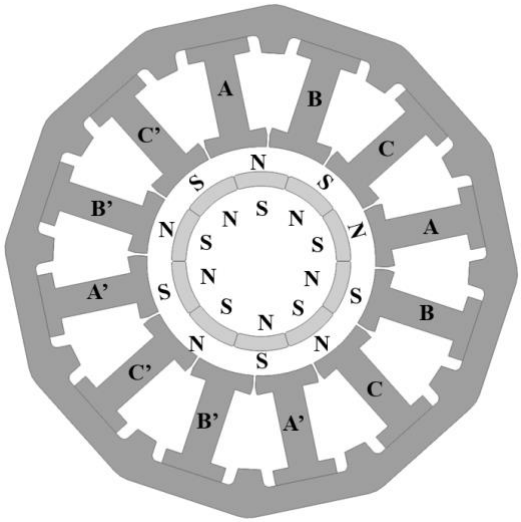

Figure 11. Schematic of 12 tooth, 3 phase BLDC motor with an inner rotor core containing 10 permanent magnets.

The rotor would not move if all three phases of the stator were excited at the same time, and each phase must be properly excited to maximize torque. This requires BLDC motors to have three phase control and sensing of the rotor position.

Refer again to Figure 11, where it can be seen that the north pole of the rotor is positioned near phase A. When operating, the rotor is going to make a full 360º rotation back to phase A to achieve its desired rotational application, i.e. move water through a cooling system. This is done by exciting each pole to oppose and attract the north and south pole of the rotor. Figure 12 shows a typical excitation sequence for a three-phase BLDC motor.

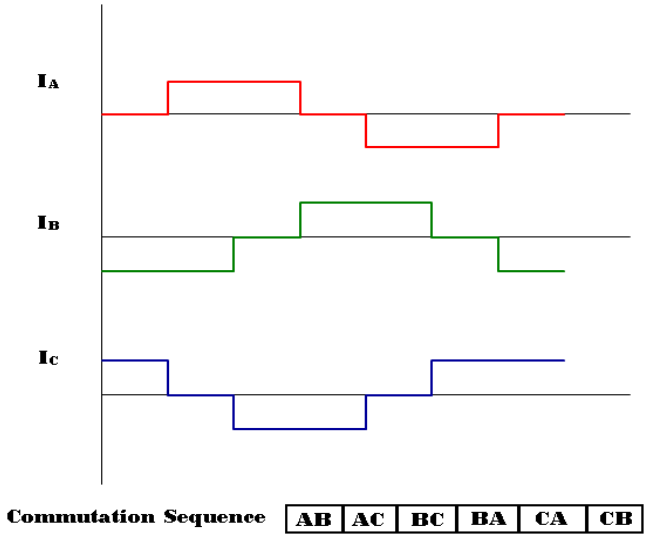

Figure 12. Commutation sequence for a three-phase BLDC motor

2.3.1 *Governing Equations*

Now that the stator and the rotor are defined, we can begin to develop equations for the motor operation. A basic design construction for the size of a motor is given by the Equation 2.9 where k is a constant, D is the rotor diameter, and L is the axial rotor length [40].

$$T = kD^2L \tag{2.9}$$

One of the most important operations for the motor is the amount of torque created from the stator and rotor. Torque can be derived from the basic physics of Equation 2.10.

$$P = Fv \tag{2.10}$$

where power, P, is equal to the amount of work done per unit time. However, our system is confined to the rotation, so the Power/Torque equation used is shown in Equation 2.11 where ω is the rotational speed in mechanical radians per second.

$$P = T\omega \tag{2.11}$$

To find the torque developed by this motor, the electrical properties of the stator and rotor must be taken into consideration. The mutual inductance of the stator windings and the generation of the magnetic fields affect how the motor generators its torque. The total flux for the system is defined by Equation 2.12.

$$\begin{bmatrix}\varphi_a\\ \varphi_b\\ \varphi_c\end{bmatrix} = \begin{bmatrix}L_{aa} & L_{ab} & L_{ac}\\ L_{ba} & L_{bb} & L_{bc}\\ L_{ca} & L_{cb} & L_{cc}\end{bmatrix}\begin{bmatrix}i_a\\ i_b\\ i_c\end{bmatrix} + \begin{bmatrix}\varphi_{am}\\ \varphi_{bm}\\ \varphi_{cm}\end{bmatrix} \tag{2.12}$$

where $\varphi_a, \varphi_b, \varphi_c$ are the total fluxes linked between each stator winding, L_{aa}, L_{bb}, L_{cc} are the self-inductances of the stator windings, $L_{ab}, L_{ab}, L_{ba}, etc.$ are the mutual inductances between each phase of the stator windings, and $\varphi_{am}, \varphi_{bm}, \varphi_{cm}$ are the fluxes from the permanent magnets linking the stator windings. The inductances are a function of the rotor angle and are defined below as Equation 2.13 where M_s is the average stator mutual inductance between the stator windings.

$$\begin{aligned}
L_{aa} &= L_s + L_m\cos(2\theta r),\\
L_{bb} &= L_s + L_m cos(2(\theta r - \tfrac{2\pi}{3})),\\
L_{cc} &= L_s + L_m cos(2(\theta r + \tfrac{2\pi}{3})),\\
L_{ab} = L_{ba} &= -M_s - L_m cos(2(\theta r + \tfrac{\pi}{6})),\\
L_{bc} = L_{cb} &= -M_s - L_m cos(2(\theta r + \tfrac{\pi}{6} - \tfrac{2\pi}{3})),\\
L_{ca} = L_{ac} &= -M_s - L_m cos(2(\theta r + \tfrac{\pi}{6} + \tfrac{2\pi}{3})),
\end{aligned} \tag{2.13}$$

These inductances are used to calculate the total flux, which is then transformed to the DC plane using the Park's transformation. The torque can then be calculated by Equation 2.14.

$$T = \frac{3}{2}N\left(i_q i_d L_d - i_d i_q L_q\right) + \begin{bmatrix} i_a & i_b & i_c \end{bmatrix} \begin{bmatrix} \frac{d\varphi_a}{d\theta_r} \\ \frac{d\varphi_b}{d\theta_r} \\ \frac{d\varphi_c}{d\theta_r} \end{bmatrix} \tag{2.14}$$

Chapter 3. SYSTEM DESIGN

The pump itself contains three main parts: 1) an inner rotor which contains herringbone grooves to move fluid and create a pressurized fluid bearing, 2) a watertight chassis that holds the rotor and pumping fluid and 3) the outer stator coils that provide a rotating magnetic field that drives the pump's rotor. The design of these three parts is discussed in detail in the following parts of this chapter with an additional section outlining other hardware that was used in creating the full fluid circulation loop. A summary section concludes this chapter.

3.1 PUMP ROTOR

The pump rotor was designed to mimic the form factor of a journal bearing, that is to say, the rotor is cylindrical in shape. This allowed for stability adding herringbone grooves to be applied to the outer edge of the rotor and the assumption that the established literature on the fluid flow properties of the herringbone grooves could be applied. The herringbone groove design is discussed in section 3.1.1 of this chapter. With the basic shape of a herringbone grooved journal bearing in place an internal modification was made, inside of the rotor permanent magnets were installed to interact with the external stator and generate a magnetic field to rotate the rotor and in turn pump fluid. The internal magnet design is discussed in section 3.1.2. In addition to the internal derivations of a journal bearing, two external modifications were also made 1) 4 fins were added to the end of one of the cylinder faces and 2) a hole was cut through the center to increase fluid flow and pumping ability of the rotor. These designs were modeled in the Computer Aid Design (CAD) software SOLIDWORKS and the logic decisions of the design are found in 3.1.3

3.1.1 *Herringbone Grooves*

The application of herringbone grooves onto journal bearings is a practice that has evolved from simply being applied to large machinery to more recently being used in miniature rotating machines with applications in a diversity of industries ranging from automotive and aerospace to computer hardware. Previous studies involving herringbone grooves on journal bearings has focused on the geometry optimization and theoretical simulation. One constant theme running throughout the current body of research is the manufacturing techniques employed to create such

grooves. All other empirical work on herringbone grooves involved various material removal processes such as high-speed lathe cutting or etching. With one of the goals of this project being to manufacture parts using 3D printing technology a study into 3D printed herringbone grooves had to be conducted. This study is discussed later in detail in section 4.1.1 of this thesis. It was this experimental process of printing a 72-part matrix of herringbone groove parameters that lead to the design for the herringbone grooves used on the pump rotor.

The final herringbone groove geometry chosen for the pump rotor was a bevelled-step due to how this shape was the most constantly reproduced by 3D printers. Also, as discussed in section 2.2.2 the bevelled-step geometry has a higher load carry capacity and lower frictional torque than the square herringbone groove geometry. A groove depth of 500 μm was chosen due to consistent reproducibility between the 3D printed result and CAD design. This groove depth, in turn, leads to a 333 μm distance between the pump's rotor and chassis surfaces. Given this design the minimum number of grooves was calculated using Equation 2.7 and Equation 2.8 and due to the small size of the rotor and assuming an internal ambient pressure within the groove of 5 psi with an angular velocity of 300 rpm and using Koolance Liquid coolant as the lubricant for everything operating at 20 °C the bearing compressibility number was found to be 1.15726 with a minimum number of grooves being 0.2314 [50].

3.1.2 *Internal Permanent Magnets*

In order for the pump's rotor to both levitate and rotate to pump fluid permanent magnets had to be incorporated into the rotor design, thus creating an inner rotor geometry for the brushless DC motor design. After testing 13 different types of magnets ranging in pull force, shape, size and material, a neodymium arc magnet with a nickel-copper-nickel coating made by CMS magnets was selected. Five of the ten magnets in the circular array are magnetized through the thickness with the north pole on the inner diameter, the other five magnets are also magnetized through the thickness but have a south pole on the inner diameter. The ten pieces of this arc magnets form a circle with an outer diameter of 1.5 inches, an inner diameter of 1.25 inches, and a height of 0.75 inches. Additional information about the magnetic characteristics of the magnets can be seen outlined in Table 3-1.

Table 3-1. Magnetic characteristics of the Neodymium arc magnets inside the Rotor		
	Value	Unit
Gauss Rating:	13, 200	Gauss
H_{cb}:	13.24	KOe
H_{cj}:	13.42	KOe
(BH)max:	39.5	Mega Gauss Oersteds, MGOe
Working Temperature:	150	°C

A CAD design of the magnets was created and then used to specify the size of the internal cutout shell space of the rotor. The rotor design also was split into two parts so that magnets could be placed inside the shelled-out area once the part was 3D printed. It was found that the cutout area for the magnets had to be 120% the size of the magnets due to printing tolerances.

3.1.3 *Design*

The design of the rotor is such that it acts as an inner rotor for the brushless DC motor stator located on the outside of the chassis. Incorporating the design elements reviewed at the beginning of this chapter as well as herringbone grooves and permanent magnets discussed in previous sections of this thesis the final rotor design can be seen in Figure 13.

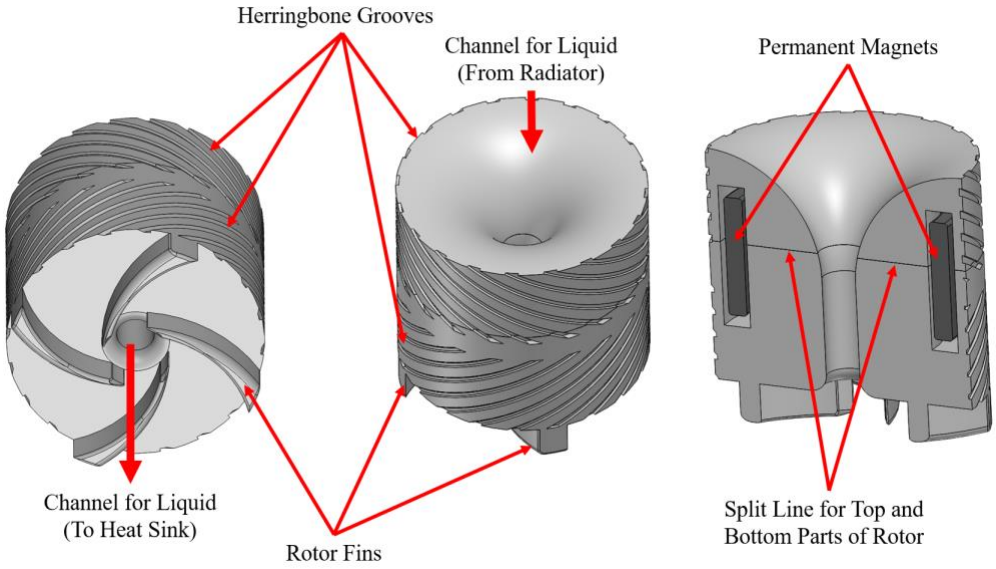

Figure 13: Overview of the rotor design highlighting herringbone groove stability design features, rotor fins, and coolant flow direction through the shaftless rotor.

The permanent magnets could not be incorporated into the rotor while it was being 3D printed so the body of the rotor was split to create two pieces. The location of the split was chosen so that the herringbone grooves would easily be aligned when the two parts were connected again. A CAD model of the part as a whole and two parts can be seen in Figure 14.

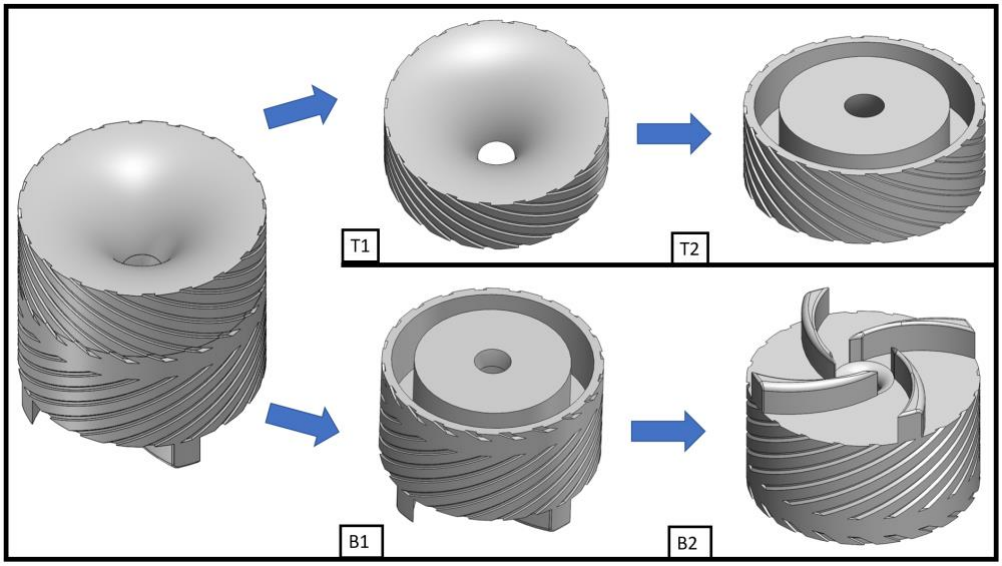

Figure 14: CAD images of the rotor as one piece and then split to create a top and bottom piece T1) the top piece of the split rotor in the same orientation as the whole rotor piece T2) Upside down view of T1 B1) the bottom piece of the split rotor in the same orientation as the whole rotor B2) Upside down view of B1

The overall height of the rotor is 49.13 mm (~1.93 in) with the rotor fins being 5.75 mm (~0.23 in) resulting in the journal bearing part of the rotor is 43.38 mm (~1.71 in). The outside diameter of the rotor is 43.38 mm (~1.71 in) this yields in the wall between the outside of the permanent magnet assembly ring to be 1.96 mm (0.08 in). A wall thickness less than this was found to be too thin given the herringbone groove depth while still maintaining structural integrity while a thicker wall was not wanted due to the added resistance that would be created by the additional material. The slots for the permanent magnets had to be increased in size by 110% from the size of the permanent magnets due to 3D printing tolerances. The hole that cuts through the rotor is 6.35 mm (~0.25 in) in diameter.

3.2 CHASSIS

3.2.1 *Water Retention Testing and Material Selection*

For the chassis to function properly it needs to hold fluid without leaking. Thus, testing was undertaken to check the fluid retention properties of the different 3D printed materials at

different printer layer resolution settings. The ASTM D570-98 (2010) standard was followed to test water retention with all three of specified geometry types being 3D printed using FDM technology in 20, 50, 100, and 200-micron resolution, in both PLA and ABS plastic [51]. These prints were created using the Ultimaker 2+, and the CreaterPro 2 printer for polylactic acid (PLA) and Acrylonitrile butadiene styrene (ABS) material. These materials were chosen due to known material properties, cost, and availability. A photograph of some of the created specimen can be seen in Figure 15.

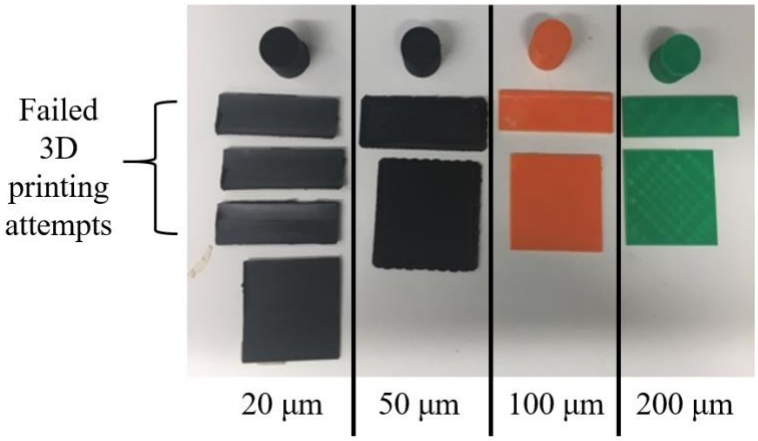

Figure 15. A photograph showing the PLA plastic 3D print specimens organized by 3D printing layer resolution in all three ASTM D570-98 (2010) standard sizes.

Failed results for all samples tested proved that if manufacturing the chassis was going to be done using a 3D printing technique a post-process step would be needed to eliminate the possibility of any liquid leaks.

In order to waterproof 3D printed PLA an epoxy adhesive, Loctite 29314, Hysol E-20 HP was used. This specific epoxy was chosen by recommendation of Stratasys, a leading rapid prototyping company, to seal FDM parts [52]. The two-part epoxy was mixed and applied to the edges of a chassis. Tests spanning 10 days were conducted on different samples to determine the number of surfaces of the part the epoxy had to be applied (inside surface, outside surface, inside and outside surfaces). Leaks were observed when the epoxy was applied to only the outside layer of a part, but when the epoxy was applied to the inside layer of a part (or both the inside and outside layer of a part) the part did not leak. This method was undesirable due to the lack of control

available, even when great care was being used, in the applied coat's layer is even. An uneven buildup of epoxy was noticed, and the inside of the walls had noticeable ridges. Such ridges in the chassis that will be serving as a journal housing is unacceptable as it could cause chaotic fluid flow and failure of the pump system.

To waterproof, a 3D printed ABS part a "Smoothing Station" was created [52]. This station consisted of a large glass case, magnets, and paper towels that had been saturated with acetone inside of a fume hood. The paper towels were attached to the inside of the glass case using magnets, after allowing vapors to form for 5 minutes the glass cage was lifted and an ABS 3D printed part was laid inside. After waiting for 10 minutes the part was removed. The acetone vapors melted the layers of ABS plastic together resulting in smooth walls that were also watertight. Due to the ease of this method as well as desirable results the selection of ABS plastic filament was chosen to print the Chassis design with the added post-processing step of a smoothing station.

3.2.2 *Design*

The design of the chassis consists of three sections that span two separate parts, a lid and a base. A CAD image of the design with both parts as well as the three sections can be seen in Figure 16. The chassis lid contains the first section of the chassis, the fluid inlet section. Fluid will enter the chassis from this point and continue down into the second part of the chassis. In the second part of the chassis, the base, the fluid will be pumped around the edges and through the pump's rotor which is housed inside of the chassis - this is the transition phase of the chassis.

There are many types of heat sinks that are readily available for purchase and that could fit within the form factor of the chassis design with small changes to the chassis base. Since this is a proof of concept prototype surrounding the operation of the pump the step of integrating a heat sink is out of the scope of this thesis. Simulations of the fluid flow in the chassis is also an area for future work and are discussed at length in section 5.2.1.2 of this thesis.

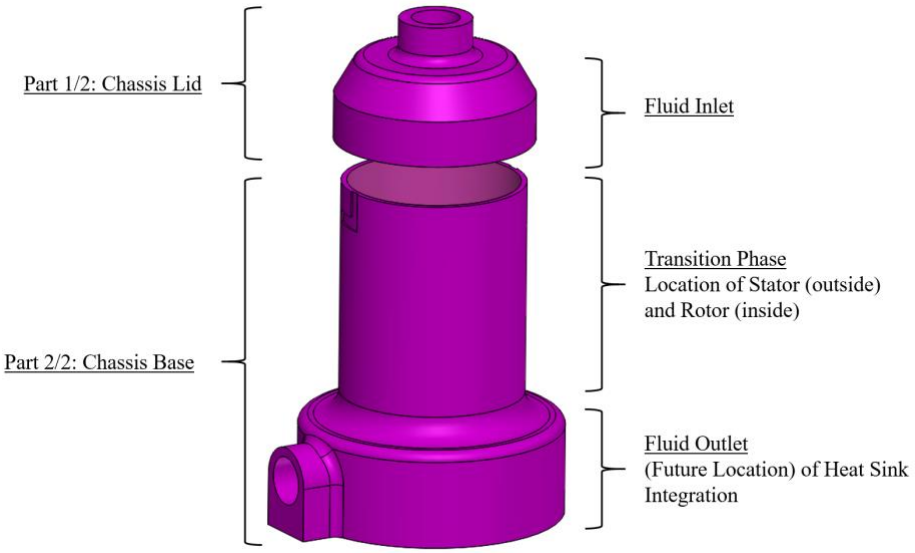

Figure 16. Design of the chassis with parts and major sections outlined.

From the transition phase section of the chassis, the fluid enters the final part of the chassis, the fluid outlet section. The fluid outlet section is a circular section that was designed for easy integration of a heat sink. It is intended that the cold fluid would flow around an integrated heat sink that in turn is in contact with a high heat component found in a server board. After the liquid has absorbed heat from the heat sink it will flow from the chassis base to a radiator that will remove the heat and cycle the cooling fluid back to the chassis.

The dimensions for this chassis base transition phase was chosen based on compatibility with the rotor design dimensions and to minimize the gap between the permanent magnets inside the rotor and the stator coils. Knowing that the distance between the outside rotor wall and the chassis wall needs to be 333 μm given the 500 μm groove depth ideally the inside diameter of the chassis would be about 43.38 mm, but because of dimensional shrinkage that occurs due to a combination of ABS material properties as well as using 3D printing, the dimensions that yielded in the desired results had to be found empirically by trial and error. The inside diameter of the rotor dimension that leads to a 333 μm gap between the rotor and the edge of the chassis is 44.5 mm (~1.75 in) and with a wall thickness of 1.5 mm (~0.06 in) the outside diameter of the rotor is 46 mm (~1.81 in).

For the chassis base fluid outlet section, the base of the chassis was increased to provide a stand for the stator when installed. It also created a location for a future integration of a heat sink

if wanted. The chassis base has an outer diameter of 68.28 mm (~2.69 in). The inlet and outlet sections of the chassis were designed to fit connectors described in Section 3.4. A CAD model section view of the chassis can be seen in Figure 17.

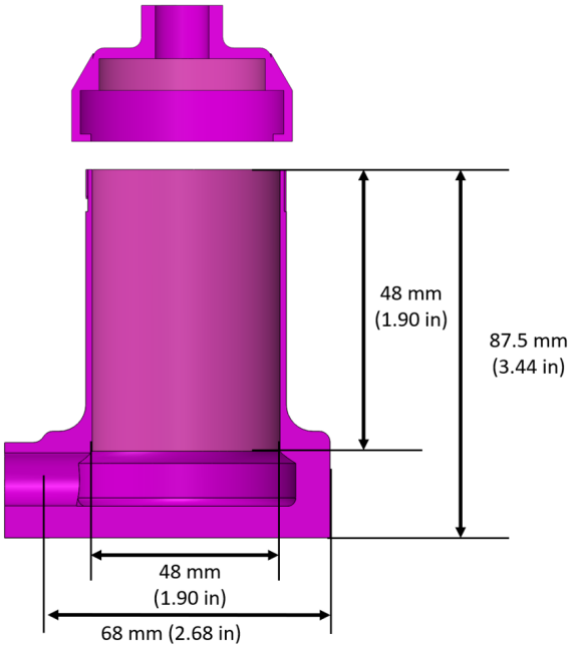

Figure 17. Front section view of the chassis CAD model showing top, front, and orthogonal views of the final stator assembly design with key dimensions noted.

3.3 STATOR

3.3.1 *Stacked Steel Shim Design*

For building motor stators, low-carbon steel is an ideal choice of material [53]. This is because carbon decreases magnetic permeability in the material, and causes magnetic aging, causing power loss over time. Stators are also typically constructed using laminated steel, and with multiple teeth layers tightly compressed together using lamination, a process called impregnation [54, 55]. By fixing together layers of steel instead of using solid blocks, the eddy current induced in the steel by the varying magnetic field of the coils is reduced. This current generates a magnetic field which opposes the field generated by the coils, reducing power, so minimizing the eddy current maximizes efficiency. With this in mind, a first iteration of a stator was designed and

constructed using two rolls of $12"$ x $120", 0.006"$ thick, 1008-1010 low-carbon steel shim stock were purchased from McMaster-Carr. The stator cross-sections were cut using a Kern 300 DPI Laser cutter located at the Center for Experimental Nuclear Physics and Astrophysics Laboratory (CENPA). The production of layers was automated to produce 16 stator cross-sections per cut job. 16 was chosen as the optimal number of cross-sections per cut job due to the physical restriction given by the length of the laser cutter table. In total, 44 layers were printed from a single roll of $12" \; x \; 120"$ steel shim, with a total of 72 layers being cut with the fully optimized laser settings. After the layers were cut the process of impregnating the layers was looked into and found to be too expensive and time consuming for a single proof-of-concept prototype. To compensate for this the stator was connected on the outside layers using adhesive tape and then wound using Remington Industries 24SNSP 24AWG Magnet Wire. Using the winding method for a three-phase brushless direct current (DC) motor the wire was wrapped around the stator as can be seen in Figure 18 [56].

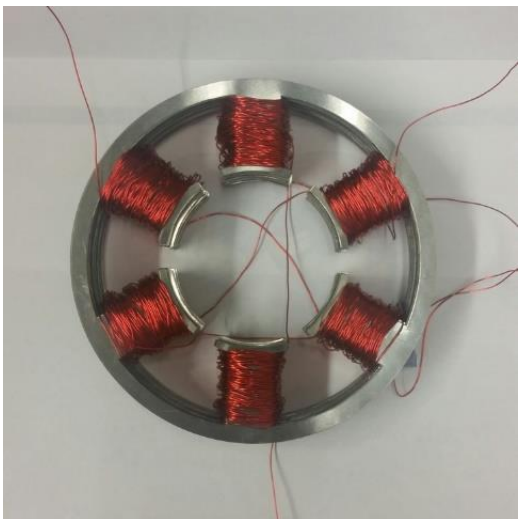

Figure 18. Photograph of the 6 teeth first iteration design where 72 steel shims were stacked to create the body of the stator.

Once this was completed it was found that the stator did not commutate at all when connected to the TI-DRV8313EVM controller. After performing troubleshooting, it was determined that the coils were shorted to the stator layers, a continuity check between coil windings and stator stack identified shorts on all coils. A photograph of this phenomenon can be seen in

Figure 19. The second attempt of this design was made to fix these problems including re-wiring the stator and adding more protection around the coils for the wire, but after a second failed to attempt another method to prototype the stator was investigated. Additionally, the design was updated to a twelve-tooth design so that the gap between the teeth was reduced to aid in stability of the rotor while spinning within the chassis.

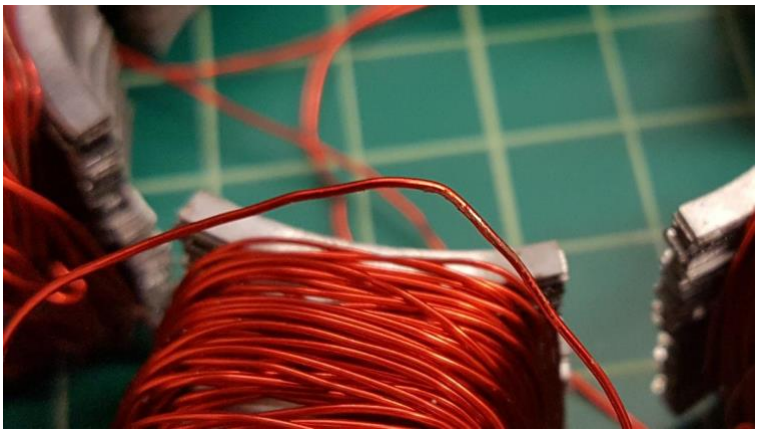

Figure 19. Close up photographs of wire insulation on stator removed from rough edges of the stator

3.3.2 *Iron Composite PLA Design*

A ferromagnetic composite PLA 3D printing filament was discovered to be made by the manufacturer ProtoPasta. The magnetic properties of the PLA are shown in Table 3-2 and were used to print the stator frame, teeth, and rotor core. Stator winding remained a wye configuration. While the innovation space around composite 3D printing filaments is still relatively young, this particular manufacturer's product has been referenced and used successfully in both hobby and academic settings to create electronic components [57].

Table 3-2 Properties of Proto-pasta's magnetic Iron Metal PLA Composite	
Induction at magnetic saturation	0.15 Tesla
Relative Permeability (to air)	5 – 8 H/m independent to frequency up to 1MHz
Permeability	62E-7 to 100 E-7 H/m

To facilitate with connecting the stator teeth to the stator frame and to increase the amount of steel in the stator, M6-1 X 20 mm ISO 4762 Hex Drive Class 12.9 black oxide finish alloy steel

socket cap screws were integrated into the stator design. These design decisions allowed for the stator design the be modular to facilitate ease of assembly and 3D printing. A CAD model of the stator was created to ensure dimensional accuracy of the assembly. A section view of the final assembly with the 1) stator teeth 2) stator frame and 3) black oxide bolts pointed out can be seen in Figure 20.

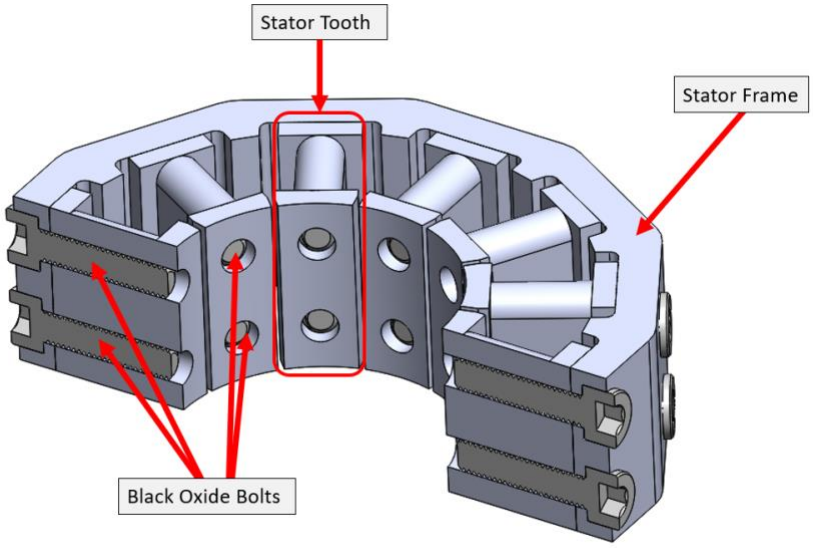

Figure 20. Solidworks CAD model of stator cross section

The twelve teeth are each 22.85 mm (~0.90 in) in length, the inside diameter of the stator where the chassis fits into is 48 mm (~1.90 in), the outside diameter of the stator is 105 mm (~4.14 in). A CAD model of the top, front, and orthogonal views of the stator assembly with coils can be seen in Figure 21.

A 16 AWG annealed bare copper magnetic wire with a Polyamide imide insulation was purchased by the manufacturer CNC Tech for use in the stator coils. The wire is designed to be used in windings for electric equipment and has a usage rating of 200 °C which is safely beyond the thermal limits of the high-reliability pump.

When winding the copper coils in the stator a distributed-Lucas, Retzbach, and Kuhfuss (LRK), or dLRK, winding scheme was used. This scheme was used due to the modular format, and how it requires fewer copper windings per stator tooth [58]. Given the small footprint desired by the high-reliability pump design this winding scheme is ideal. The winding pattern in turn for

the stator is AabBCcaABbcC where the lowercase letters imply reverse, counter-clockwise, turns in the winding direction.

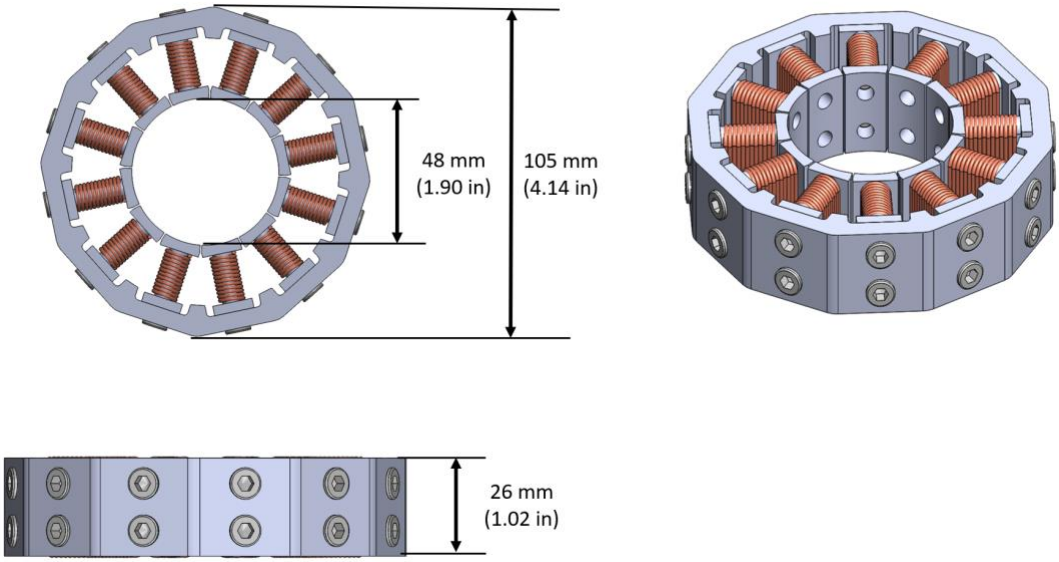

Figure 21. Images of the CAD model showing top, front, and orthogonal views of the final stator assembly design with key dimensions highlighted.

3.4 Pump System's Fluid Circulation Loop

The following materials were used to create a fluid circulation loop that had a built-in flow meter. The components were chosen based on cost, availability, and intended use for a computer liquid cooling solution.

Connectors. An elbow fitting was deemed necessary to reduce the bending strain on the tubing connecting to the side of the pump chassis. The model selected is a single rotational angled fitting barb for 1/4in (6mm) inner diameter tubing. Its brass material with nickel plating proved to be one of the lightest weight options, adhering to a critical design consideration. Its dimensioning was selected to fit with the pump design. This fitting includes a hose clamp design to connect with the tubing.

Tubing. Koolance clear polyurethane tubing with 1/4in (6mm) inner diameter and 3/8in (10mm) outer diameter was ordered to fit the dimensions of the previously selected fittings. With the proposed pump assembly in mind, the tubing selection needed to have some ability to bend.

This tubing has a bend radius of approximately .98in (25mm), placing it in the flexible category, ideal for the design.

Flow Meter. The INS-FM16 Coolant flow meter was selected as the flow meter for the coolant loop due to its accuracy of ±5% and flow rate range of 0.5-15 liters per minute. A Koolance DCB-FM01 flow meter adapter was also used to output the flow rate from the flow meter. A custom stand was also designed, and 3D printed to hold the flow meter and flow meter adapter in final testing of the high-reliability pump which can be seen in Figure 31.

Radiator. A Thermaltake Aqua TMG1 120mm radiator was connected using the earlier defined plastic tubing and a G1/4'' connector that press fit into the tubing for a leak-proof connection. An image of the radiator that highlights the inlet location for the warm liquid and the outlet location of the cooled liquid can be seen in Figure 22. The material for the tube and fins is aluminum with a zinc coating applied to limit corrosion and has a high-density fin design to accommodate the 93 cubic feet per minute air flow generated by the attached fan.

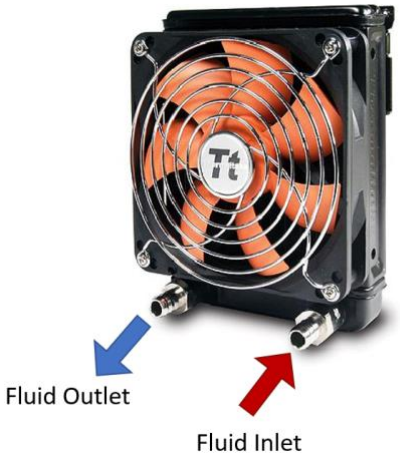

Figure 22. Photograph of the Thermaltake Aqua TMG1 radiator with inlet and outlet locations identified

Overall, the design of the pump assembly and fluid loop as it would be seen in a server board can be seen as a CAD image in Figure 23.

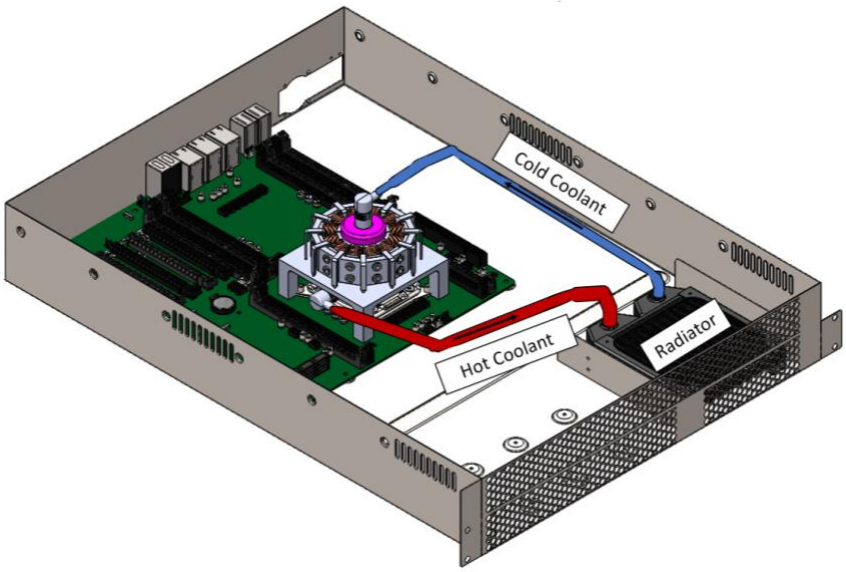

Figure 23: Assembled view of the proposed pump design installed on a motherboard in a server.

3.5 SUMMARY

In conclusion, the design for the pump assembly was created and modeled using the 3D CAD software SOLIDWORKS. The back and forth between the design and the resulting 3D printed part proved to be a challenge but was overcome through many iterations only possible because of the low cost and readily available use of 3D printing technology. The overall design intent with an integrated heat sink on a computer high heat electronic component can be seen in Figure 24. Major design components of the system are again outlined and the flow of the cold fluid into the pump and then being turned over the heat sink, collecting heat, and then flowing out of the pump assembly into the fluid loop are also pointed out.

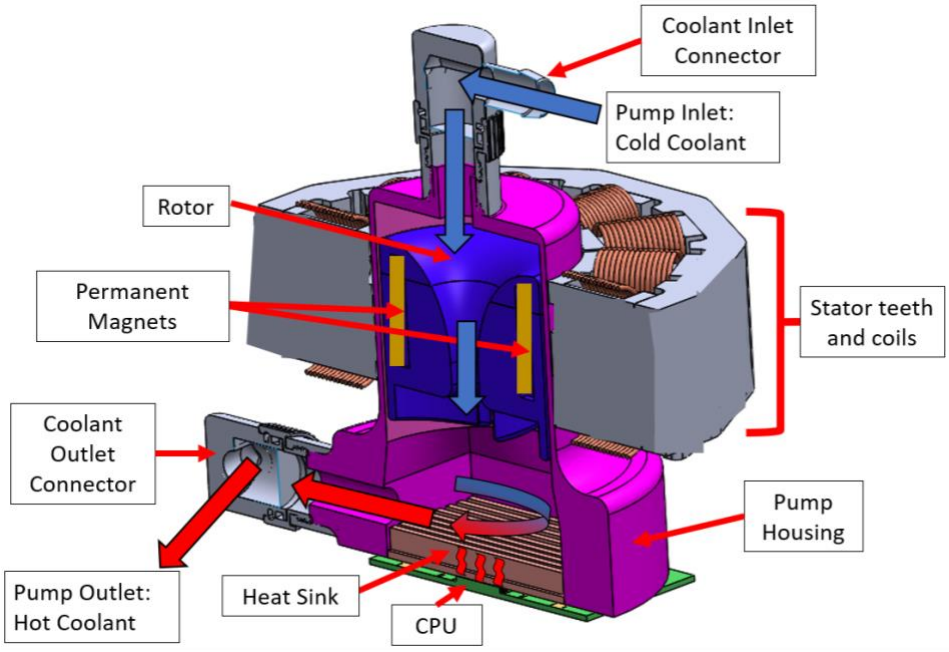

Figure 24: A 3D computer aid design section view of the pump design, outlining key design components and highlighting the heat transfer between the CPU and the fluid flowing through the pump's assembly.

Chapter 4. SYSTEM EXPERIMENT

4.1 MATERIALS AND METHODS

The pump rotor, chassis and prototype parts are produced using the additive manufacturing technology of fused deposition modeling 3D printing. Later stages beyond the scope of this project can address manufacturing of parts using injection molding.

4.1.1 *Three-Dimensional Printing*

To test how different 3D printing technologies layer resolutions affected the resulting quality of herringbone grooves a Stratus' Object30 Pro, Ultimaker's Ultimaker 2+, and Stratus' Dimension 1200es printers were used. Object30 Pro is an industrial grade prototyping machine that uses PolyJet technology similar to inkjet printers where two liquid photopolymer materials, the main material and a support material, are sprayed onto a platform one layer at a time with an ultraviolet light following the nozzle thus curing the material [14]. A support material is used during the PolyJet manufacturing process to aid in printing tall parts and to provide an initial building platform. The Ultimaker 2+ and the Dimension 1200es printers use the most common method of printing, Fused Deposition Modeling (FDM) [15]. Plastic FDM involves taking a spool of plastic filament and feeding it through a heated nozzle that melts the material. The curing process between layers for FDM is simply the plastic cooling in the time between being ejected from the nozzle and the placement of the subsequent layer [16]. Table 4-1outlines the 3D printers, materials, and the printing resolutions used in this study.

None of the 3D printing methods investigated required a post-curing process after the build is complete, but the removal of support material is needed. A custom small power washing station that can be seen in Figure 25 was used to remove the Objet Support SUP 707. An SCA (Support Cleaning Apparatus)-1200 filled with a sodium hydroxide solution was used to remove Soluble Support Technology (SST) Support Material. It was found that a low powered pressure washer, that can be seen in Figure 25, removed most of the support material, but residue could be seen and felt on the edges that had been coated with the support material during the printing process.

Removal of the SST support material using the SCA-1200 machine proved successful without any residue post cleaning cycle.

Table 4-1. 3D Printers Used for Prototypes

Manufacturing Company	**Stratus**	**Ultimaker**	**Stratus**
Printer model	Objet30 Pro	Ultimaker 2+	Dimension 1200es
Main Material	VeroClear	Polylactic Acid (PLA)	Acrylonitrile butadiene styrene (ABS)
Support Material	Objet Support SUP707	None	Soluble Support Technology (SST)
Layer Print Resolution	16 µm	60 µm 100 µm	250 µm

Figure 25: Photograph of the power washing station used to remove Objet Support SUP707 material from samples printed using PolyJet technology.

To assess the effect that 3D printing resolution has on herringbone groove geometries, 16, 60, 100, and 200 micrometer 3D printer resolution were used in printing square, circular, and bevelled step herringbone groove geometries. Three herringbone grooves depths of 225, 300 and 500 micrometers were 3D printed at a 16, 60, 100, and 250-micrometer printing layer resolution

totaling 36 test samples for both the cylindrical and flat parts to create a matrix of 72 samples in total. Due to key herringbone groove parameters relying on ratios between groove depth and the clearance between journal bearing and retaining outer wall, each set of printed herringbone groove models has a specific journal clearance that ensures optimal load bearing capacity of the grooves. The optimal journal clearance (H_r) and associated groove depth (H_g) for each printed are outlined in Table 4-2.

Table 4-2. Outline of Square, Circular, and Beveled-Step Herringbone Groove Depths and Journal Clearance

Depth of Groove (H_g)	Key Parameters	Square Groove (µm)	Circular Groove (µm)	Beveled-Step Groove (µm)
225 µm	Journal Clearance (H_r)	204.5	225	150
300 µm	Journal Clearance (H_r)	273	300	200
500 µm	Journal Clearance (H_r)	454.5	500	333

Each of the defined optimum herringbone grooves was placed on both a cylinder and flat surface. This was done so that if a pattern didn't resolve satisfactorily in a given print resolution, one could determine if it was because of the added complexity of printing on a curved surface that caused the failure, or if it was due to other manufacturing variables. The cylinder shape resembles that found in a journal bearing, thus it will be the focus of analysis and how the design for the herringbone grooves on the pump rotor will be decided.

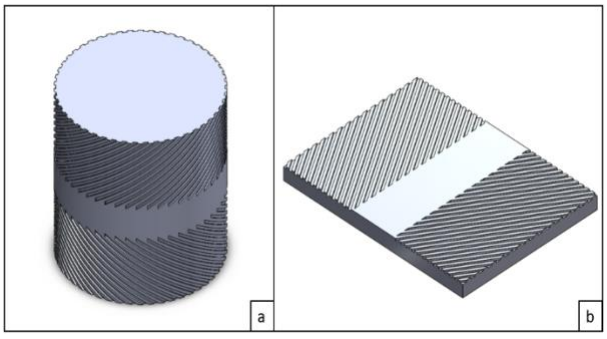

Figure 26: Orthogonal views of the two 3D CAD model geometries printed (a) cylinder and (b) square models for square herringbone grooves.

4.1.2 *Optical Images of Parts*

A Starrett KineMic KMR-200-M3 Video Microscope was used to inspect and take images of the 3D printed parts. Using a lens magnification of 0.7X images were taken at both ends of the cylinder, as this is a critical location for lubrication to flow through and around the rest of the journal bearing. Table 4 shows a comparison for what this different end profiles were designed to look like from the CAD model, and how it actually turned out at the three different printing layer resolutions used.

Given that surface roughness can affect lubricant flow parts were inspected to see if the printed layers would be visible and possibly cause an adverse effect. The parts were tilted on their sides and viewed at magnification levels ranging from 0.7X to 7.5X. For the high-resolution parts built using the PolyJet method, the edges appeared as a smooth solid, with no noticeable layers seen at a 7.5X magnification level. The printing layers were noticeable for both the flat and journal geometries of the lower resolution parts printed using the FDM method. These ridges can be seen in Fig. 4 for a square groove printed at a 100 µm layer resolution.

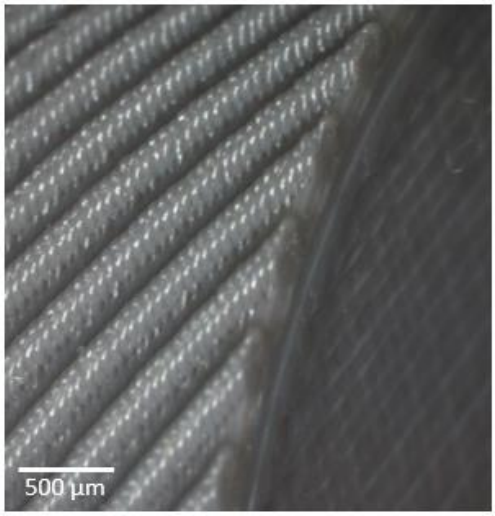

Figure 27: Optical image of tilted FDM square herringbone groove part printed at a 100 µm layer resolution.

Additional observations were made towards the center of the parts to verify the integrity of the herringbone groove geometry. For Object30 Pro printed parts (16 µm resolution), support material residue could be seen filling the grooves. When a filing tool was run inside the groove the

support material became granular but removable with a soft bristle brush. The left side of Fig. 5 shows the support material after a tool was used, and the right side shows the groves with support material still embedded.

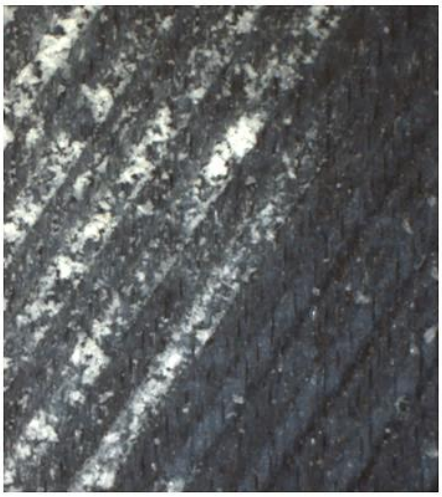

Figure 28: Image highlighting granular support material in herringbone grooves.

Square and bevelled-step groove profiles towards the center of the cylinder for the medium and low-resolution prints can be seen in Figure 28. The circle groove profile was not included in the image because from the top view where the images were taken at the circular groove profiles was indistinguishable from the square groove profiles.

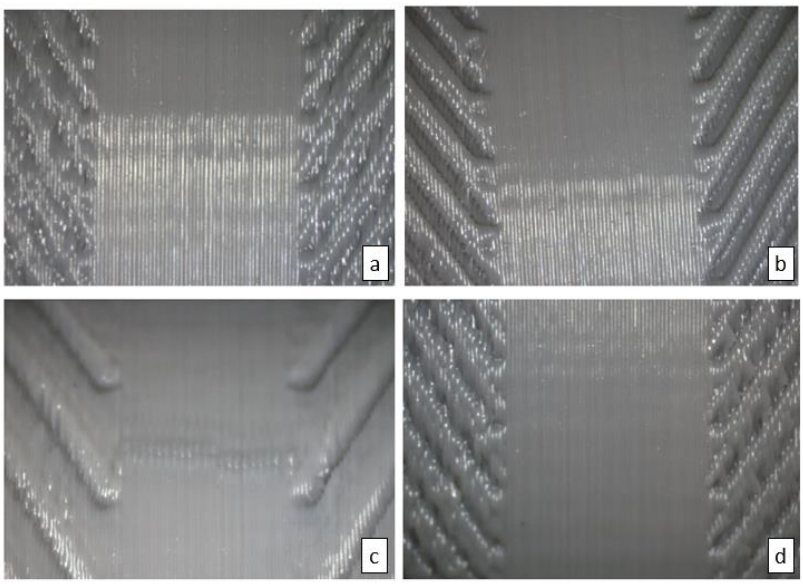

Figure 29. Images of medium and fine-resolution FDM herringbone groove parts (a) 60 µm bevelled-step groove (b) 60 µm square groove (c) 100 µm resolution bevelled-step groove (d) 100 µm resolution square groove.

From viewing the groove geometries at the end of the cylinder outlined in Table 4 it can be seen, as expected, that the highest resolution print, using PolyJet technology, ended up mimicking the CAD model best. Although this is a promising discovery for the possibility expanding the current range of methods to create a journal bearing with herringbone grooves, the fact that the support material was so tedious to remove from the grooves leaves to question if having a method that requires so much post-processing is a viable solution. The use of lower resolution print is seen to be possible, but only if the groove depth ratio and layer resolution are at least built at a one-to-three ratio.

4.2 Experimental Setup

In this section, the experimental set up results of functional testing the pump assembly system is completed. A photograph of the pump's stator, chassis, and rotor can be seen in Figure 30. The chassis is flipped upside down and the bottom is cut out so that the rotor positioned inside of the chassis can be seen.

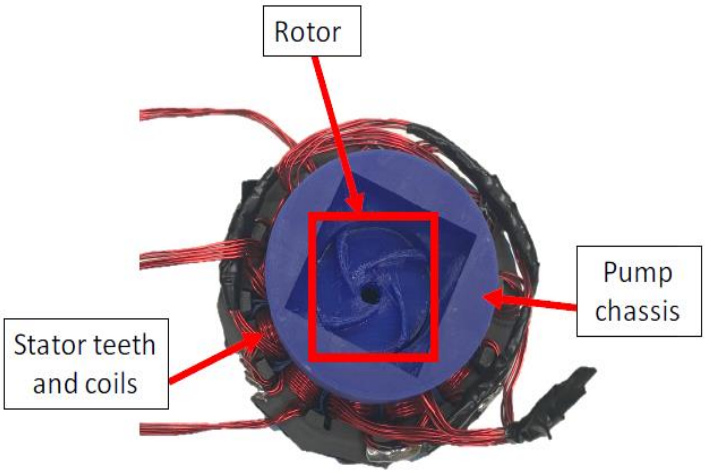

Figure 30: Photograph of the liquid cooling pump tilted upside down and with a section of the chassis base removed to highlight the pump's rotor.

The laboratory bench set up used for functional testing can be seen in Figure 31 with key components outlined.

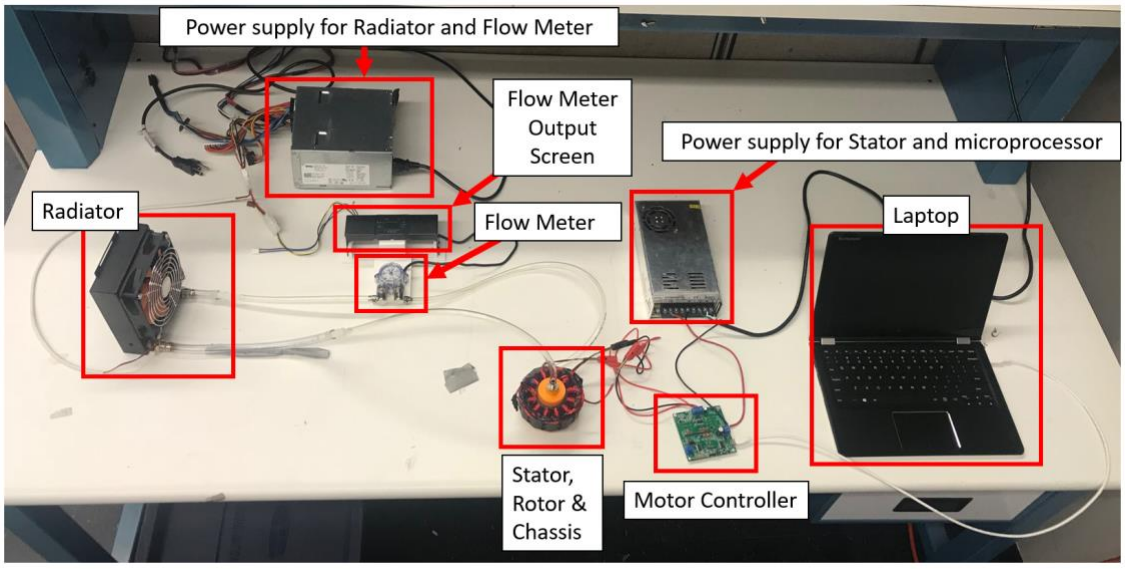

Figure 31: Photograph of the experimental setup for testing the proof-of-concept prototype

4.3 Results and Discussion

All the final prototype parts were printed using an Ultimaker 2+ FDM 3D printer machine. The Ultimaker Cura software was used to generate the code used by the printer to create the parts. Specific settings for different parts as well as a discussion on surface roughness can be seen in the following section of this thesis. A nozzle with 0.40 mm diameter was used for all 3D printed parts.

4.3.1 *Surface Roughness of 3D Printed Parts*

Through the current investigation, Bhaskar et al.'s results on surface roughness on hydrodynamic journal bearings were used in the analysis of the surface roughness created by the 3D printing layers [59]. Bhaskar et al. investigated an array of different surface roughness orientations and found the load carrying capacity to increase by 52.57 percent as compared to journal bearings without surface roughness, giving thought to how surface roughness induced from 3D printing may be beneficial for the application of 3D printing herringbone grooved journal bearings. A stylus method MARSURF XR 20 MIT GD 25 roughness measuring station was used to collect surface roughness data of the side of a 3D printed cylinder part. The part was printed using the same specifications for the pump chassis which included a 0.40 mm nozzle, ABS 2.85 mm plastic filament with printing parameters of a 6 µm step size in the ΔZ direction. Measurements were taken for the sample before and after the vapor chamber post-process treatment, but because the part was never used without the process, and there was a clear difference in surface roughness between the parts before and after the acetone vapor chamber. The resulting measurement can be seen in Figure 32.

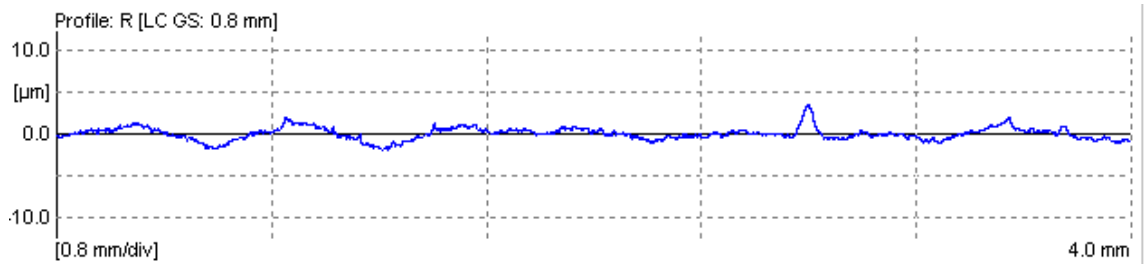

Figure 32. Graph of surface roughness for the chassis with a found surface roughness value, Ra, of 0.562 µm and mean deviation of the 3D printed layers from the nominal height of 3.229 µm.

The found roughness is small enough that it did not interfere with the operation of the pump during functional testing. Further work could look into methods to decrease the roughness even more by using a 3D printer nozzle with a smaller diameter or decreasing the layer height.

4.3.2 *Pump Rotor*

The pump rotor design was successfully 3D printed. Photographs of the bottom part of the rotor can be seen in Figure 33.

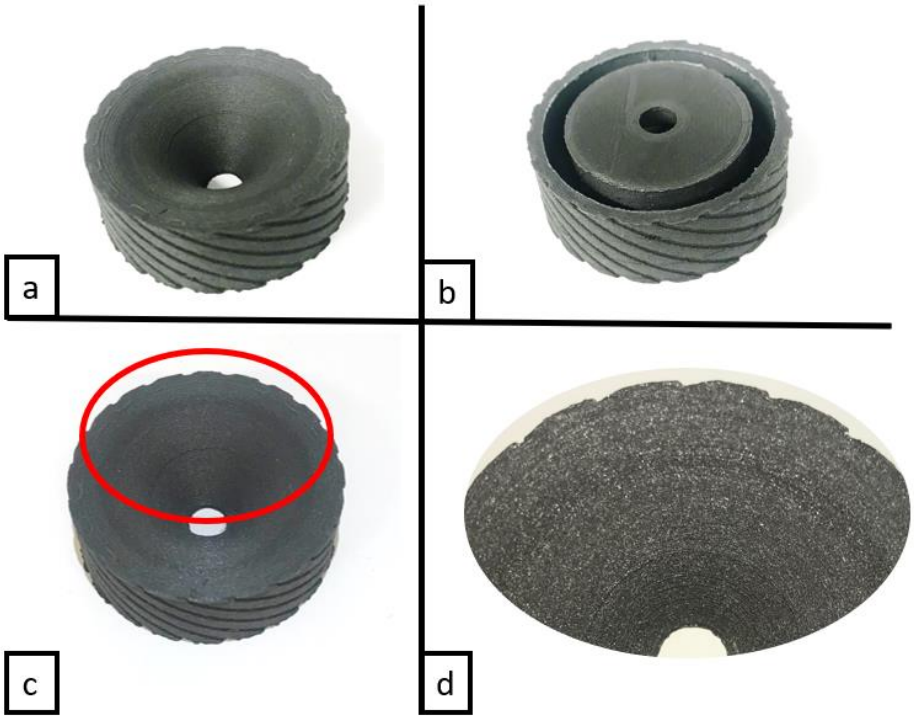

Figure 33. Images of the final rotor prototype showing a) the top half of the rotor b) the top half of the rotor flipped upside down c) the top half of the rotor with section d) close up of the rotor showing the detail of print for the bevelled-step herringbone grooves.

It was found that the optimum printing settings for creating a quality print included a build plate temperature of 65 °C, and a material flow rate of 100%. No support material or build plate was used as it was found that incorporating these features lead to the first few layers of the 3D print having warped herringbone groove profiles. Additionally, it was found that in order to avoid the first few layers of the print from peeling off of the build plate surface the controls had to be tuned for the first few layers. For the first layer in the print, the nozzle temperature was set to 220

℃ and print speed of 50%. For the second layer in the print, the nozzle temperature was decreased to 210 °C while the print speed was increased to 70%. After the second layer, the 3D printer settings were set to their final set of a nozzle temperature of 200 ℃ and a print speed of 100%. A 0.1mm layer height was used as well as an 80% material infill. When printing the rotor parts took a total of 8 hours and 30 minutes and consumed about 44 grams of the composite iron PLA filament.

4.3.3 *Pump Chassis*

When printing the chassis, the nozzle temperature was set to 230 ℃, the build plate temperature was set to 65 ℃, and a material flow rate of 100%. A 0.10 mm layer height with a 30 % material infill was used. It took 17 hours and 57 minutes to print the part which consumed 58 grams of ABS material. A build plate was used for this print as it was found that if a build plate was not selected that the print layers would be uneven from shifting on the build plate. Once the print was complete the nozzle spouts for the inlet and outlet tube connections needed to be tapped using a drill bit. Finally, an enclosure had to be built around the top of the 3D printer to insulate and regulate the temperature inside the build area. When the enclosure was not used the dimensions of the part were inaccurate by ± 30 µm.

Figure 34. Photograph of the final chassis prototype

4.3.4 *Pump Stator*

It was found that the same tuning adjustments made when printing the pump's rotor regarding the nozzle temperature and print speed needed to be applied when printing the stator components. The hex bolts were able to be screwed into place by simply using the appropriately sized hex key, so no tapping of the parts was necessary. Once the stator was coiled the ends of the phases were soldered together in parallel so that the order of the connection would only change the direction of rotation of the rotor, but not cause one of the phases to be skipped over, or out of sequence. Just like in the case of the rotor, the stator had a 0.1 mm layer height and 80% infill which lead to the printing time of the stator assembly to take 23 hours and 10 minutes and consuming 102 grams of material. A photograph of the final stator prototype with coils can be seen in Figure 35.

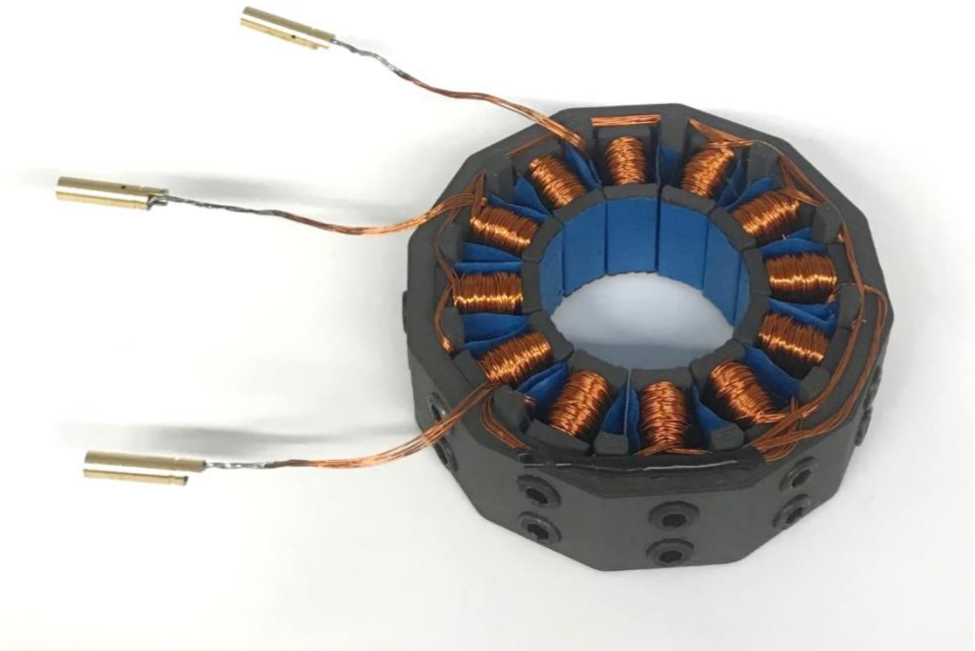

Figure 35. Photograph of the final 3 phase brushless DC motor stator prototype

4.3.5 *Pump Fluid Assembly*

The pump's fluid assembly successfully functioned without leaks during the duration of the functional tests. The fluid used for all experiments was tap water. Due to the system not being filled underwater or in a vacuum environment, there were bubbles in the system, but because of the low flow rates and relatively low rotational speed of the pump's rotor no cavitation effect was noticed. A detailed discussion on cavitation is discussed in Section 5.2.1.1 of this thesis. Since there is no source of heat in the system the liquid didn't change temperature during the experiments. The temperature was measured using a digital pocket thermometer from Grainger with an accuracy of ± 1 °C.

4.3.6 *Functional Testing*

Using the experimental setup shown in Figure 31 the entire pump assembly was tested for the basic function of the proof-of-concept prototype. Using an Arduino Uno microcontroller and readily available code for operating the 3-phase stator. A HiTEC ESC power supply which supports up to 28 VDC and 20 amps provided power to the controller while 2 Velleman PSIN30024N power supplies sent power to the stator, flow meter, and radiator. Given the bounds for the fluid flow meter was a minimum flow rate of 0.5 L/min the first speed of the rotor that yielded in a noticeable flow rate was at a rotor speed of 150 rpm. Once the settings were changed for a speed five minutes of time was waited to make sure that the fluid would be accurately read by the flow meter and to ensure that the pump could operate at that new speed. The pump was tested at increments of 10 rpm increases from 150 rpm to 300 rpm. Within this speed range, the prototype was tested on three separate days with all three days of testing showing similar results. Analysis past 300 rpm was not completed because at this speed the rotor magnets tended to shift out of position inside the rotor on day two of testing. It was found that if glue was applied this issue went away, but nevertheless testing beyond this bound can be done in the future to see the limits of the system beyond the scope of the functional tests completed for this thesis. The tabular data collected can be seen in Appendix B. In Figure 36 a graph of the data collected on Day 1 of functional testing can be seen. The coefficient of determination, R^2, shows that the data follows a linear trend very well with a value of $R^2 = 0.9929$.

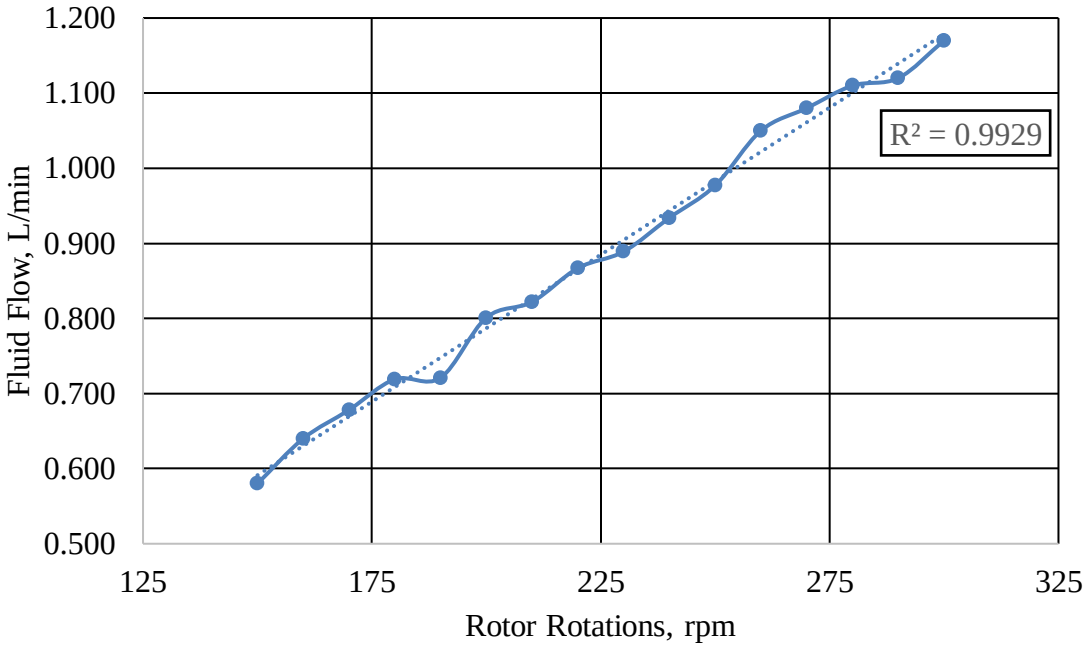

Figure 36. Graph of the functional data collected on Day 1 of testing the prototype

Chapter 5. CONCLUSIONS AND FUTURE WORK

5.1 CONCLUSIONS

In conclusion, a design for a high-reliability pump was created for the end use application of liquid cooling high heat electronic components found in a data center's server board. A review of the fundamental concepts for liquid cooling, herringbone grooves, and brushless DC motors introduced the design parameters and previous work done on the technologies that were integrated into the pump system's design. A proof-of-concept prototype of the design was fabricated and subsequently tested. The pump's rotor, chassis, and stator were created using the FDM 3D printing technique. Innovative use of iron composite PLA filament allowed for a magnetic field to be created and interact with permanent magnets housed inside the pump's rotor. This lead to the successful adoption of a pump rotor that levitated and rotated inside of the chassis without the typical shaft design. The prototyped pump was successfully tested for functionality and found to be able to pump water through the fluid loop.

Regarding intellectual property currently associated with this thesis, a U.S. Provisional Patent Application No. 62/205,345 was filed in August 2016, and a utility patent was filed in August 2016.

5.2 FUTURE WORK

This section outlines future work and identifies potential next steps for this project from both a research and commercialization viewpoint. The information outlined is not intended to be an exhaustive list, but rather to present observations and information gathered by the author over the course of this project for consideration.

5.2.1 *Research*

5.2.1.1 Cavitation Effects

A numerical simulation on the effects of cavitation on herringbone grooves was studied in 2000 by Jang et al. and concluded that the cavitation region on a journal increases with a *decrease* of the groove width ratio and *increase* of the journal's length to diameter ratio (L/D), eccentricity,

rotational speed and groove angle [43]. The shortcoming of this research paper is that only a square herringbone groove geometry is considered. With the advances in different herringbone groove shapes since its publication, including the circular and bevelled-step groove profiles discussed in this thesis, an updated analysis on the topic would be advantageous. Additionally, beyond possible cavitation effects in the herringbone groove region of the pump system, research into possible cavitation effects on the rotor fins could be explored.

5.2.1.2 Multiphysics Simulations

A multiphysics simulation that encapsulated the computational fluid mechanics, heat transfer, rotor dynamics and electromagnetic forces of the pump system would be beneficial to understand the system's limits and for any future design optimization efforts. Given the novelty of using magnetic iron composite PLA filament for manufacturing a brushless DC motor's stator and rotor, a multiphysics simulation that evaluated the coupling of heat transfer and electromagnetic forces in relation to the material structural properties would aid in the understanding the limits of using such material for other applications.

5.2.1.3 Electronic Insulation

The magnetic field of the rotor's permanent magnets and the stator's windings that extend beyond the boundaries of the DC cooling fan have the potential to create a uniform magnetic field environment. Due to how the high-reliability pump is located directly on the server board, insulation of the pump assembly would protect the server board data storage components from potential failure caused by interference. Given this, when the pump is in close proximity to IT equipment including a server board, the use of high permeability magnetic shielding material should be used to eliminate any possible interference.

There are many types of shielding that could be integrated into the design for future design iterations. Board-Level Shielding (BLS) is a common shielding method used to eliminate electromagnetic interference (EMI) radiation in a printed circuit board. This type of shielding contains a solder-attached perforated metal can soldered to the ground trace on a printed circuit board directly over the electrical components that need to be shielded. The metal can consist of tin or zinc plated steel, stainless steel, tin-plated aluminium, brass, copper beryllium, nickel silver or other copper alloys [60]. Board-Level Shielding is most commonly used in mobile electronics such as smartphones and tablets. Because spacing between components on PCBs is being reduced

in wireless devices, new EMI shielding solutions are being created for the PCB level. Another shielding method that could be included is thermoformed board-level shields. This method is becoming increasingly popular because they eliminate unwanted space and are lighter in weight than traditional soldered cans [61]. Ferrite materials are used when dealing with noise such as in noise filters. Their performance is similar to high permeability metals, but they have lower intrinsic magnetic noise generated because of their high resistivity [62]. Because of their ability to control the magnetic flux, ferrite sheets or spray coating ferrite materials can provide effective protection in applications such as power transfer and near field communication [63].

5.2.2 *Commercialization*

Foreseeable future steps that need to take place to translate this thesis's high-reliability pump into a commercially available product are reviewed in this section.

5.2.2.1 Field Test

Once extensive reliability testing has been completed, field testing the pump inside a data server environment should be done. This testing could include multiple setups including different server size configurations (1 Rack Unit (RU), 2 RU, 4 RU, etc.) as well as the server's installed inside different server cabinets and in turn different server cabinet row. Ideally, the field testing would be completed in an active data center environment. Bringing the testing into the field has been shown to can provide confidence to both customers and engineers as the setting for testing and end-use application is equivalent [64]. Hence, the testing could also be used in marketing efforts for promoting the pump to potential future clients.

5.2.2.2 Mass Production Strategy

For this product to be mass produced a strategy would need to be formed. This strategy would have to include manufacturing, material and component sourcing, as well as distribution. An example of a manufacturing aspect of this project that would need to be investigated is the cost versus benefits associated with 3D printing items such as the stator. At a mass production, scale being able to manufacture the stator using traditional methods could benefit the product by increasing the efficiency of the system and decrease the power consumption needed to operate the

pump assembly. This strategy would have to include both business and engineering components as the pump demand scaled.

5.2.2.3 Remote User Control

At a point where this design was to be mass-produced and installed in data center server board, sensors and controls should be added so that a data center operations technician could easily control and monitor the thermal management systems. Also, in a worst-case scenario of a pump assembly failing, the remote user control could alert a technician so that the problem could be corrected in a timely manner and reduce the possibility of crucial high heat components failing due to overheating. Such technology has been previously explored and patented by companies like Hewlett Packard and Schneider Electric IT Corporation, but a novel way to accomplish this task could lead to further intellectual property [65-68].

5.2.2.4 Intellectual Property

Although a patent has already been submitted for the design of the pump, the additional intellectual property surrounding the method to manufacture the pump rotor could be advantageous for commercialization and license the technology.

BIBLIOGRAPHY

[1] J. Koomey, "Growth in data center electricity use 2005 to 2010," *A report by Analytical Press, completed at the request of The New York Times,* vol. 9, 2011.

[2] J. G. Koomey, "Worldwide electricity used in data centers," *Environmental research letters,* vol. 3, no. 3, p. 034008, 2008.

[3] Z. Song, X. Zhang, and C. Eriksson, "Data Center Energy and Cost Saving Evaluation," *Energy Procedia,* vol. 75, pp. 1255-1260, 2015/08/01 2015.

[4] P. Delforge and J. Whitney, "Issue Paper: Data Center Efficiency Assessment Scaling up Energy Efficiency Across the Data Center Industry: Evaluating Key Drivers and Barriers," *Natural Resources Defense Council (NRDC),* 2014.

[5] H. Coles and S. Greenberg, "Direct Liquid Cooling for Electronic Equipment," Ernest Orlando Lawrence Berkeley National Laboratory, Berkeley, CA (US)2014.

[6] M. S. Williams, K. J. Longmuir, and P. Yager, "A practical guide to the staggered herringbone mixer," *Lab on a Chip,* vol. 8, no. 7, pp. 1121-1129, 2008.

[7] H. Bliss, "What is an Active Heatsink?," *Wise Geek,* Blog 2018.

[8] E. Banks, "Cisco ASA: High CPU in Dispatch Unit," *Packet Pushers Interactive,* Blog 2013.

[9] A. C. Kheirabadi and D. Groulx, "Cooling of server electronics: A design review of existing technology," *Applied Thermal Engineering,* vol. 105, pp. 622-638, 2016.

[10] Z. Liu *et al.,* "Renewable and cooling aware workload management for sustainable data centers," in *ACM SIGMETRICS Performance Evaluation Review,* 2012, vol. 40, no. 1, pp. 175-186: ACM.

[11] N. Ahuja, "Datacenter power savings through high ambient datacenter operation: CFD modeling study," in *Semiconductor Thermal Measurement and Management Symposium (SEMI-THERM), 2012 28th Annual IEEE,* 2012, pp. 104-107: IEEE.

[12] A. Kumar, "Thermal Management Technologies for Semiconductor Microchips," (in English), *BCC Research,* Market Research Report 2017, Art. no. SMC106A.

[13] K. Ebrahimi, G. F. Jones, and A. S. Fleischer, "A review of data center cooling technology, operating conditions and the corresponding low-grade waste heat recovery opportunities," *Renewable and Sustainable Energy Reviews,* vol. 31, pp. 622-638, 2014.

[14] A. H. Bonnett, "Root cause AC motor failure analysis with a focus on shaft failures," *IEEE transactions on industry applications*, vol. 36, no. 5, pp. 1435-1448, 2000.

[15] F. Berndt and A. Van Bennekom, "Pump shaft failures—a compendium of case studies," *Engineering Failure Analysis*, vol. 8, no. 2, pp. 135-144, 2001.

[16] A. H. Bonnett, "Understanding motor shaft failures," *IEEE industry applications magazine*, vol. 5, no. 5, pp. 25-41, 1999.

[17] S. V. Garimella, L.-T. Yeh, and T. Persoons, "Thermal management challenges in telecommunication systems and data centers," *IEEE Transactions on Components, Packaging and Manufacturing Technology*, vol. 2, no. 8, pp. 1307-1316, 2012.

[18] G. Hirs, "The load capacity and stability characteristics of hydrodynamic grooved journal bearings," *ASLE transactions*, vol. 8, no. 3, pp. 296-305, 1965.

[19] E. Rasmussen, P. Rudolph, and A. Mamishev, "An Experimental Study of 3D Printed Herringbone Grooved Journal Bearings," in *ASME 2017 International Mechanical Engineering Congress and Exposition*, 2017, pp. V007T09A083-V007T09A083: American Society of Mechanical Engineers.

[20] H. E. Ahmed, B. Salman, A. S. Kherbeet, and M. Ahmed, "Optimization of thermal design of heat sinks: A review," *International Journal of Heat and Mass Transfer*, vol. 118, pp. 129-153, 2018.

[21] X. Meng, J. Zhu, X. Wei, and Y. Yan, "Natural convection heat transfer of a straight-fin heat sink," *International Journal of Heat and Mass Transfer*, vol. 123, pp. 561-568, 2018.

[22] S. Lee, "Optimum design and selection of heat sinks," in *Semiconductor Thermal Measurement and Management Symposium, 1995. SEMI-THERM XI., Eleventh Annual IEEE*, 1995, pp. 48-54: IEEE.

[23] M. Saini and R. L. Webb, "Heat rejection limits of air cooled plane fin heat sinks for computer cooling," *IEEE Transactions on Components and Packaging Technologies*, vol. 26, no. 1, pp. 71-79, 2003.

[24] K.-Q. Ma and J. Liu, "Nano liquid-metal fluid as ultimate coolant," *Physics Letters A*, vol. 361, no. 3, pp. 252-256, 2007.

[25] S. C. Mohapatra and D. Loikits, "Advances in liquid coolant technologies for electronics cooling," in *Semiconductor Thermal Measurement and Management Symposium, 2005 IEEE Twenty First Annual IEEE*, 2005, pp. 354-360: IEEE.

[26] J. Cho and B. S. Kim, "Evaluation of air management system's thermal performance for superior cooling efficiency in high-density data centers," *Energy and buildings*, vol. 43, no. 9, pp. 2145-2155, 2011.

[27] E. R. Masanet, R. E. Brown, A. Shehabi, J. G. Koomey, and B. Nordman, "Estimating the energy use and efficiency potential of US data centers," *Proceedings of the IEEE*, vol. 99, no. 8, pp. 1440-1453, 2011.

[28] S. Greenberg, E. Mills, B. Tschudi, P. Rumsey, and B. Myatt, "Best practices for data centers: Lessons learned from benchmarking 22 data centers," *Proceedings of the ACEEE Summer Study on Energy Efficiency in Buildings in Asilomar, CA. ACEEE, August*, vol. 3, pp. 76-87, 2006.

[29] M. Fonteccio. (2008). *Limiting Vibrations in Data Center Design*. Available: http://searchdatacenter.techtarget.com/news/1297628/Limiting-vibrations-in-data-center-design

[30] E. Sampino. (2014). *Vibration Isolation in Data Centers*. Available: https://www.slideshare.net/securetechnicalrooms/vibration-isolation-35651682

[31] I. Shen, "Recent vibration issues in computer hard disk drives," *Journal of Magnetism and Magnetic Materials*, vol. 209, no. 1-3, pp. 6-9, 2000.

[32] T. Jintanawan, I. Shen, and K. Tanaka, "Vibration analysis of fluid dynamic bearing spindles with rotating-shaft design," *IEEE transactions on magnetics*, vol. 37, no. 2, pp. 799-804, 2001.

[33] E. I. Rivin, "Vibration isolation of precision equipment," *Precision Engineering*, vol. 17, no. 1, pp. 41-56, 1995.

[34] C. Alhan and H. P. Gavin, "Reliability of base isolation for the protection of critical equipment from earthquake hazards," *Engineering Structures*, vol. 27, no. 9, pp. 1435-1449, 2005.

[35] R. Schmidt, "Structural and Vibration Guidelines for Datacom Equipment Centers," in *ASHRAE Datacom Series*, R. a. A.-C. E. American Society of Heating, Ed., ed, 2008, p. 193.

[36] N. Zirkelback and L. San Andres, "Finite element analysis of herringbone groove journal bearings: a parametric study," *Journal of tribology*, vol. 120, no. 2, pp. 234-240, 1998.

[37] J. K. Vennard, *Elementary fluid mechanics*. Read Books Ltd, 2013.

[38] N. Rieger, "Design of Gas Bearings. Vol. I: Design Notes. Mechanical Technology," ed: Inc, 1966.

[39] R. Whipple, "The inclined groove bearing," United Kingdom Atomic Energy Authority. Research Group. Atomic Energy Research Establishment, Harwell, Berks, England1958.

[40] J. H. Vohr and C. Y. Chow, "Characteristics of herringbone-grooved, gas-lubricated journal bearings," *Journal of Basic Engineering*, vol. 87, no. 3, pp. 568-576, 1965.

[41] A. Gad, M. Nemat-Alla, A. Khalil, and A. Nasr, "On the optimum groove geometry for herringbone grooved journal bearings," *Journal of Tribology*, vol. 128, no. 3, pp. 585-593, 2006.

[42] G. Jang and J. Yoon, "Nonlinear dynamic analysis of a hydrodynamic journal bearing considering the effect of a rotating or stationary herringbone groove," *TRANSACTIONS-AMERICAN SOCIETY OF MECHANICAL ENGINEERS JOURNAL OF TRIBOLOGY*, vol. 124, no. 2, pp. 297-304, 2002.

[43] G. Jang and D. Chang, "Analysis of a hydrodynamic herringbone grooved journal bearing considering cavitation," *Journal of Tribology(Transactions of the ASME)(USA)*, vol. 122, no. 1, pp. 103-109, 2000.

[44] N. Zirkelback and L. San Andres, "Finite element analysis of herringbone groove journal bearings: a parametric study," *TRANSACTIONS-AMERICAN SOCIETY OF MECHANICAL ENGINEERS JOURNAL OF TRIBOLOGY*, vol. 120, pp. 234-240, 1998.

[45] K. Kinouchi and K. Tanaka, "Performance Characteristics of Herringbone-Grooved Journal Bearings Using a Finite Element Method," in *Proceedings of the Japan International Tribology Conference*, 1990, pp. 935-940.

[46] D. Bonneau and J. Absi, "Analysis of aerodynamic journal bearings with small number of herringbone grooves by finite element method," *Journal of Tribology*, vol. 116, no. 4, pp. 698-704, 1994.

[47] K. Kang, Y. Rhim, and K. Sung, "A study of the oil-lubricated herringbone-grooved journal bearing—part 1: numerical analysis," *Journal of tribology*, vol. 118, no. 4, pp. 906-911, 1996.

[48] J. H. Vohr, and Chow, C. Y, , "Characteristics of Herringbone-Grooved Gas-Lubricated Journal Bearings," *ASME J. Basic Eng*, vol. 87, pp. 568-578, 1965.

[49] D. P. Fleming and B. J. Hamrock, "Optimization of self-acting herringbone journal bearing for maximum stability," 1973.

[50] Koolance, "Koolance 702 Liquid Coolant, High-Performance, UV Blue, 700ml (24 fl oz)," Website 2018, Art. no. Part No. LIQ-702BU-B

[51] A. Standard, "D570-98 (2010) e1, Standard test method for water absorption of plastics, ASTM International, West Conshohocken, PA," ed.

[52] Stratasys, "Sealing FDM Parts," *Stratasys Application Brief,* Application Brief 2015.

[53] C.-l. Xia, *Permanent magnet brushless DC motor drives and controls*. John Wiley & Sons, 2012.

[54] T. Murakami and T. Murakami, "Stator core, an electric motor in which it is utilized, and method of manufacturing a stator core," ed: Google Patents, 2005.

[55] J. Nakano, "Stator laminate impregnation in a liquid-cooled motor," ed: Google Patents, 1987.

[56] J. R. Hendershot and T. J. E. Miller, *Design of brushless permanent-magnet machines*. Motor Design Books, 2010.

[57] P. F. Flowers, C. Reyes, S. Ye, M. J. Kim, and B. J. Wiley, "3D printing electronic components and circuits with conductive thermoplastic filament," *Additive Manufacturing,* vol. 18, pp. 156-163, 2017.

[58] T. A. Johnson *et al.*, "Development and Evaluation of a Sandia Cooler-based Refrigerator Condenser," Sandia National Laboratories (SNL-CA), Livermore, CA (United States)2015.

[59] S. U. Bhaskar, M. M. Hussain, and M. Y. Ali, "Stability analysis on plain journal bearing with effect of surface roughness," *International Journal of Scientific & Engineering Researc,* vol. 4, pp. 1-8, 2013.

[60] F. Gary, "The Basic Principles of Shielding," *InCompliance,* 2014.

[61] J. F. Gabower, "Electromagnetic interference shield for electronic devices," ed: Google Patents, 1998.

[62] S. C. Tang, S. Hui, and H.-H. Chung, "Evaluation of the shielding effects on printed-circuit-board transformers using ferrite plates and copper sheets," *IEEE Transactions on Power Electronics,* vol. 17, no. 6, pp. 1080-1088, 2002.

[63] C. J. Tracy, E. Chen, M. Durlam, T. Zhu, and S. N. Tehrani, "Stray magnetic shielding for a non-volatile MRAM," ed: Google Patents, 1999.

[64] D. E. Rowley, "Usability testing in the field: bringing the laboratory to the user," in *Proceedings of the SIGCHI conference on Human factors in computing systems*, 1994, pp. 252-257: ACM.

[65] H. P. Dang and S. M. Sri-Jayantha, "Remote monitoring and servicing of computer data centers," ed: Google Patents, 2008.

[66] C.-J. Yuan, "Temperature control system," ed: Google Patents, 2012.

[67] R. Friedrich and C. Patel, "Data center energy management system," ed: Google Patents, 2003.

[68] F. Charron, "Air flow management system for an internet data center," ed: Google Patents, 2004.

APPENDIX A: NOMENCLATURE

P:	Liquid Pressure [Pa]
p_a:	Ambient pressure [Pa]
ω:	Journal rotational Speed [$\frac{rad}{s}$]
μ:	Liquid viscosity [$\frac{kg}{m \cdot s}$]
R:	Journal Radius [m]
γ:	Weight density of liquid [$\frac{N}{m^3}$]
G:	Gravitational Acceleration [$\frac{m}{s^2}$]
K_L:	Head loss coefficient
O_S, O_J:	Sleeve bearing and Journal center, respectively
Θ:	Inclination angle
Γ:	Groove depth ratio
ρ:	Density [$\frac{kg}{m^2}$]
α:	Groove angle [°]
ϕ:	Bearing attitude angle [°]
$\dot{\theta}$:	Rotational speed of journal [$\frac{rad}{s}$]
θ:	Circumferential coordinate rotating with journal
t:	Time [sec]
g:	Gravitational acceleration [$\frac{m}{s^2}$]
e_X, e_Y:	Eccentricity in X and Y direction [m]
L:	Length of journal bearing [m]
L_g:	Groove length in the circumferential direction [m]
L_p:	Pitch length of the grooves in the circumferential direction [m]
$x' = R\theta, z'$:	Coordinate system fixed to grooved journal
D:	The diameter of journal bearing [m]
ε:	Eccentricity ratio

c:	Radial journal clearance at concentric position[m]
Λ:	Bearing compressibility number
$\overline{F_R}$:	Maximum Radial Stiffness
$\bar{W}$:	Load Carrying Capacity
V:	Velocity of Liquid [$\frac{m}{s}$]
T_r:	Friction Torque [N m]
M:	Mass [kg]

APPENDIX B: FUNCTIONAL TEST RESULTS

Table 5-1. Experimental Results from Day 1 of Functional Testing

Rotor Speed, RPM	Fluid Flow (L/min)
150	0.580
160	0.640
170	0.678
180	0.719
190	0.721
200	0.801
210	0.822
220	0.867
230	0.889
240	0.934
250	0.977
260	1.050
270	1.080
280	1.110
290	1.120
300	1.170

Table 5-2. Experimental Results from Day 2 of Functional Testing

Rotor Speed, RPM	Fluid Flow (L/min)
150	0.581
160	0.640
170	0.680
180	0.725
190	0.730
200	0.800
210	0.825
220	0.868
230	0.891
240	0.940
250	0.964
260	1.010
270	1.066
280	1.100
290	1.133
300	1.165

Table 5-3. Experimental Results from Day 3 of Functional Testing

Rotor Speed, RPM	Fluid Flow (L/min)
150	0.579
160	0.638
170	0.683
180	0.727
190	0.731
200	0.801
210	0.822
220	0.865
230	0.890
240	0.941
250	0.979
260	1.000
270	1.080
280	1.089
290	1.111
300	1.167